A Terminal Fe^{III}-Oxo in a Tetranuclear Cluster: Effects of Distal Metal Centers on Structure and Reactivity

Christopher J. Reed and Theodor Agapie*

Division of Chemistry and Chemical Engineering, California Institute of Technology

Pasadena, California 91125, United States, Email: agapie@caltech.edu

Supporting Information

Table of Contents

Experimental Procedures

General Considerations

All reactions were performed at room temperature in an N_2-filled M. Braun glovebox or using standard Schlenk techniques unless otherwise specified; reactions with KOH were performed in an N_2-filled VAC wetbox. Glassware was oven dried at 140 ºC for at least 2 h prior to use, and allowed to cool under vacuum. **$LFe_3(OAc)(OTf)_2$**,[1] iodosylbenzene,[2] benzyl potassium,[3] $Fe(OTf)_2 \cdot 2$ MeCN,[4] ferrocenium trifluoromethane sulfonate ([Fc][OTf]),[5] and Ph_3PCH_2[6] were prepared according to literature procedures. *N*-*tert*-butyl-1*H*-pyrazol-5-amine (HPzNHtBu) was prepared according to a modified literature procedure.[7] 18-oxygen labeled potassium hydroxide ($K^{18}OH$) was prepared by quenching a tetrahydrofuran solution of benzyl potassium (less than 1 mmol) with $H_2{}^{18}O$, and drying the resulting white suspension under vacuum. Tetrahydrofuran, CH_2Cl_2, diethyl ether, benzene, toluene, acetonitrile, hexanes, and pentane were dried by sparging with nitrogen for at least 15 minutes, then passing through a column of activated A2 alumina under positive N_2 pressure. ^{1}H spectra were recorded on a Varian 300 MHz spectrometer; ^{13}C NMR spectra were recorded on a Varian 500 MHz spectrometer. ^{1}H and ^{31}P NMR spectra in THF/C_6D_6 were recorded on a Varian 500 MHz spectrometer using solvent suppression protocols. NMR spectra collected at low temperature were recorded on a Bruker 500 MHz spectrometer. CD_3CN, C_6D_6, and CD_2Cl_2 was purchased from Cambridge Isotope Laboratories, dried over calcium hydride, degassed by three freeze-pump-thaw cycles, and vacuum transferred prior to use.

Physical Methods

Mössbauer measurements. Zero applied field ^{57}Fe Mossbauer spectra were recorded at 80 K in constant acceleration mode on a spectrometer from See Co (Edina, MN) equipped with an SVT-

400 cryostat (Janis, Wilmington, WA). The isomer shifts are relative to the centroid of an α-Fe foil signal at room temperature. Samples were prepared by mixing polycrystalline material (20 mg) with boron nitride in a cup fitted with screw cap or freezing a concentrated acetonitrile solution in the cup. The data were fit to Lorentzian lineshapes using WMOSS (www.wmoss.org).

Electrochemical measurements. CVs and SWVs were recorded with a Pine Instrument Company AFCBP1 biopotentiostat with the AfterMath software package. All measurements were performed in a three electrode cell, which consisted of glassy carbon (working; ø = 3.0 mm), silver wire (counter) and bare platinum wire (reference), in a N_2 filled M. Braun glovebox at RT. Dry acetonitrile or tetrahydrofuran that contained ~100 mM $[Bu_4N][PF_6]$ was used as the electrolyte solution. The ferrocene/ferrocinium (Fc/Fc^+) redox wave was used as an internal standard for all measurements.

X-ray crystallography. X-ray diffraction data was collected at 100 K on a Bruker PHOTON100 CMOS based diffractometer (microfocus sealed X-ray tube, Mo Kα (λ) = 0.71073 Å or Cu Kα (λ) = 1.54178 Å). All manipulations, including data collection, integration, and scaling, were carried out using the Bruker APEXII software. Absorption corrections were applied using SADABS. Structures were solved by direct methods using XS (incorporated into SHELXTL) and refined by using ShelXL least squares on Olex2-1.2.7 to convergence. All non-hydrogen atoms were refined using anisotropic displacement parameters. Hydrogen atoms were placed in idealized positions and were refined using a riding model. Due to the size of the compounds (**1** – **3**, **5**, and **6**), most crystals included solvent-accessible voids that contained disordered solvent. In most cases the solvent could be modeled satisfactorily.

Synthetic Procedures

Synthesis of 2-*tert*-butyl-isoxazolium tetrafluoroborate. 25 mL isoxazole (0.4 mol) was combined with 37 mL *tert*-butanol (0.4 mol) in a 500 mL roundbottom flask. This was cooled to -20 °C with an ice/sodium chloride bath while 160 mL tetrafluoroboric acid diethyl ether complex (1.2 mol) was added dropwise over 1 hour. After the addition was complete, the reaction was warmed to room temperature and stirred for 4 hours. Then, 100 mL Et_2O and 50 mL THF was added to the reaction and cooled to -20 °C; the resulting precipitate was collected on a glass frit, washed three times with 200 mL Et_2O and dried under reduced pressure. 60 g of 2-*tert*-butyl-isoxazolium tetrafluoroborate (72% yield) can be obtained this way; another 6 g can be obtained by cooling the filtrate and Et_2O washings to -20 °C overnight and collecting the resulting crystals (79% overall yield). ^{1}H NMR (300 MHz, $(CD_3)_2CO$): δ 1.90 (s, 9H), 7.46 (s, 1H), 9.55 (s, 1H), 9.77 (s, 1H) ppm.

Synthesis of *N*-*tert*-butyl-1*H*-pyrazol-3-amine (HPzNHtBu). This procedure was adapted from a report describing the synthesis of *tert*-butyl substituted 3-aminopyrazoles.[7] 10.0 g of 2-*tert*-butyl-isoxazolium tetrafluoroborate (47 mmol) was suspended in 100 mL EtOH in a 250 mL roundbottom flask and cooled with an ice bath to 0 °C. A solution of 4.56 mL hydrazine monohydrate (94 mmol) in 20 mL EtOH was added dropwise to the cooled flask. After complete addition, the reaction was warmed to room temperature and stirred for 30 minutes. EtOH was removed via rotary evaporation and an aqueous work up was performed with 100 mL H_2O and 3 x 100mL CH_2Cl_2, collecting the organic layers. The combined organic fractions were dried with Na_2SO_4, filtered, and dried to yield an orange oil. The crude product was purified via Kugelrohr distillation under vacuum at 90 °C. The distillate was recrystallized with Et_2O and the resulting white solid was sublimed under vacuum at 60 °C to yield 1.6 g of HPzNHtBu (24% yield). ^{1}H

NMR (400 MHz, CD_2Cl_2): δ 1.27 (s, 9H), 3.61 (br), 5.71 (d, 1H), 7.34 (d, 1H), 9.75 (br) ppm. $^{13}C\{^1H\}$ NMR (100 MHz, CD_2Cl_2): 53.28, 75.11, 118.60, 154.26 ppm (a signal for the *tert*-butyl quaternary carbon was likely not observed). Anal. calcd. (%) for $C_7H_{13}N_3$: C, 60.40; H, 9.41; N, 30.19. Found: C, 60.75; H, 9.37; N, 30.20.

Synthesis of potassium *N*-*tert*-butyl-1*H*-pyrazol-3-amine-ate (KPzNHtBu). 1.25 g *N*-*tert*-butyl-1*H*-pyrazol-3-amine (9 mmol) was dissolved in 5 mL THF. A THF solution of 1.17 g benzyl potassium (9 mmol) was added dropwise, while stirring. After 30 minutes, the reaction was concentrated to 5 mL, and the precipitate was collected via filtration. The precipitate was washed with Et_2O and dried under vacuum to yield 1.2 g KPzNHtBu as a white solid (75% yield). Anal. calcd. (%) for $C_7H_{12}KN_3$: C, 47.42; H, 6.82; N, 23.70. Found: C, 47.50; H, 6.83; N, 23.61.

Synthesis of $LFe_3O(PzNHtBu)_3Fe(OH)$ (1). 1.287 g (0.93 mmol) $LFe_3(OAc)(OTf)_2$ was suspended in THF and froze in a liquid nitrogen cooled cold well. 502.6 mg (2.83 mmol) KPzNHtBu was added with THF while the suspension was thawing. After stirring at room temperature for 1 hour, 207.0 mg (0.94 mmol) iodosylbenzene was added with THF. After 4 hours, the solvent was removed under reduced pressure. The brown solid was transferred to a coarse porosity glass frit with celite using 50 mL pentane. The desired compound was extracted using toluene until the filtrate appeared colorless. This red-brown solution was dried completely under reduced pressure; the resulting solid (1.207 g obtained) is used in the following steps assuming a molecular formula of $LFe_3O(PzNHtBu)_3$, however this could not be confirmed via X-ray crystallography due to its poor crystallinity.

110.7 mg (0.076 mmol) of the $LFe_3O(PzNHtBu)_3$ solid was dissolved in 5 mL THF. 33.0 mg (0.076 mmol) $Fe(OTf)_2$ • 2 MeCN was added with 1 mL THF. After 45 minutes, 26 mg (0.464 mmol) KOH was added as a THF suspension. After 18 hours, the reaction appeared dark blue; this

solution was transferred to a Schlenk tube and dried under vacuum at 100 °C for 1 hour. The reaction mixture is suspended in MeCN and the blue precipitate was collected over a coarse porosity frit with celite. The precipitate was washed with MeCN until the filtrate was colorless, and then dried under vacuum. The dry blue precipitate was extracted with toluene and dried under reduced pressure. This residue was recrystallized via benzene/HMDSO vapor diffusion to yield 25.7 mg (0.017 mmol; 22% yield) of **1** as a blue solid. ^{1}H NMR (300 MHz, C_6D_6): δ 123.0 (br), 64.6 (br), 56.4, 50.1, 44.1, 41.0, 24.6, 19.6, 14.2, 12.2, 4.4, 3.2, 1.7, -40.6 (br) ppm. UV-Vis (THF) [ε (M^{-1} cm^{-1})] 253 nm (5.19 x 10^4), 494 nm (3.26 x 10^3), 609 nm (3.81 x 10^3). Anal. calcd. (%) for $C_{78}H_{76}Fe_4N_{15}O_5$: C, 61.36; H, 5.02; N, 13.76. Found: C, 61.27; H, 5.40; N, 13.12.

The 18-O labeled cluster could be prepared through the analogous protocol, substituting $K^{18}OH$ for KOH. The resulting product has identical spectroscopic features to that of **1**, and was used to prepare the remaining 18-O labeled clusters (via oxidations and/or deprotonation). ESI-MS analysis was consistent with 18-O incorporation of the cluster (Figure S18).

Synthesis of [$LFe_3O(PzNHtBu)_3Fe(OH)$][OTf] (2). 265.2 mg (0.17 mmol) $LFe_3O(PzNHtBu)_3Fe(OH)$ was dissolved in 5 mL THF. This was transferred to a stirring suspension of 52.3 mg (0.16 mmol) [Fc][OTf] in 3 mL THF. After 1 hour, the reaction was concentrated under vacuum to 1 mL and 15 mL toluene was added. The reaction was stirred for 15 minutes and the resulting red-purple precipitate was collected on a coarse frit with celite and dried completely under vacuum. The red-purple solid was extracted by washing with MeCN until the filtrate appeared colorless; this solution was dried under reduced pressure. The resulting residue was recrystallized via THF/Et_2O vapor diffusion to yield 211 mg of red-purple crystals of **2** (0.13 mmol; 82% yield). ^{1}H NMR (300 MHz, CD_3CN): δ 127.2 (br), 82.1 (br), 54.4, 49.0, 22.1, 16.5 (br), 14.1, 13.8, 13.3, 10.3 (br), 8.4, 7.8, 7.3, 1.0, -4.9, -5.1, -22.8 (br) ppm. UV-Vis (ACN)

[ε (M^{-1} cm^{-1})] 243 nm (5.96 x 10^4), 328 nm (8.83 x 10^3), 503 nm (4.88 x 10^3). Anal. calcd. (%) for $C_{79}H_{76}F_3Fe_4N_{15}O_8S$: C, 56.61; H, 4.57; N, 12.54. Found: C, 56.72; H, 4.70; N, 12.03.

Synthesis of $[LFe_3O(PzNHtBu)_3Fe(OH)][OTf]_2$ (3). 102.3 mg (0.06 mmol) $[LFe_3O(PzNHtBu)_3Fe(OH)][OTf]$ was dissolved in 3 mL DCM and a solution of 20.3 mg (0.06 mmol) [Fc][OTf] in 2 mL DCM was transferred to this stirring solution. After 2 hours, 10 mL pentane was added to the reaction and the blue precipitate was collected on a coarse porosity glass frit with celite. The blue powder was dried under vacuum and extracted with DCM until colorless, and recrystallized from DCM/Et_2O to obtain 76.8 mg of **3** as blue crystals (69% yield) ^{1}H NMR (300 MHz, CD_2Cl_2): δ 144.3 (br), 103.7 (br), 82.0, 79.7, 66.0, 63.1, 15.5, 12.8, 9.9, 3.5, 1.2, -0.5, -2.3 (br), -11.6 (br) ppm. [ε (M^{-1} cm^{-1})] 238 nm (5.76 x 10^4), 345 nm (7.74 x 10^3), 634 nm (4.80 x 10^3). Anal. calcd. (%) for $C_{80}H_{76}F_6Fe_4N_{15}O_{11}S_2$: C, 52.65; H, 4.20; N, 11.51. Found: C, 51.70; H, 4.37; N, 11.11.

Synthesis of $[LFe_3O(PzNHtBu)_3Fe(OH)][OTf]_3$ (4). 42.9 mg (0.024 mmol) $[LFe_3O(PzNHtBu)_3Fe(OH)][OTf]_2$ was dissolved in 2 mL DCM and 8.1 mg (0.024 mmol) [Fc][OTf] was added with 2 mL DCM. After 30 minutes, the reaction was concentrated and 10 mL Et_2O was added to produce a green precipitate. This was collected on a frit over celite and rinsed with Et_2O. The precipitate was collected with DCM and recrystallized via vapor diffusion of Et_2O to obtain 39.0 mg (0.020 mmol; 82% yield) **4** as green crystals. ^{1}H NMR (300 MHz, CD_2Cl_2): δ 95.2, 85.0, 14.5, -1.8, -44.9. -48.3 ppm. UV-Vis (ACN) [ε (M^{-1} cm^{-1})] 242 nm (7.11 x 10^4), 355 nm (8.85 x 10^3), 748 nm (7.39 x 10^3). Anal. calcd. (%) for $C_{81}H_{76}F_9Fe_4N_{15}O_{14}S_3$: C, 49.28; H, 3.88; N, 10.64. Found: C, 49.19; H, 4.09; N, 10.02.

Synthesis of $LFe_3O(PzNHtBu)_3Fe(O)$ (5). 102.6 mg (0.06 mmol) $[LFe_3O(PzNHtBu)_3Fe(OH)][OTf]$ was dissolved in 15mL THF and froze in a liquid nitrogen

cooled cold well. 7.2 mg (0.06 mmol) KOtBu was added to the thawing solution, and the reaction was stirred at room temperature for 1 hour. The solvent was removed under reduced pressure and the crude product was recrystallized via benzene/HMDSO vapor diffusion to obtain 26.2 mg of **5** as purple crystals (0.02 mmol; 28% yield). ^{1}H NMR (300 MHz, C_6D_6): δ 105.9 (br), 58.5 (br), 55.3, 53.0, 40.9, 38.9, 33.9, 21.8, 14.4, 11.7, 2.4, 1.1, -21.5 (br) ppm. UV-Vis (THF) [ε (M^{-1} cm^{-1})] 248 nm (4.40 x 10^4), 342 nm (6.73 x 10^3), 539 nm (3.41 x 10^3). Anal. calcd. (%) for $C_{78}H_{75}Fe_4N_{15}O_5$: C, 61.40; H, 4.95; N, 13.77. Found: C, 60.04; H, 5.01; N, 13.06 (Calcd. (%) for $C_{78}H_{75}Fe_4N_{15}O_5$ • 0.5 ($C_6H_{18}OSi_2$): C, 60.05; H, 5.27; N, 13.08; compound recrystallized from benzene/HMDSO).

Synthesis of [$LFe_3O(PzNHtBu)_3Fe(O)$][OTf] (6). 50.3 mg (0.03 mmol) [$LFe_3O(PzNHtBu)_3Fe(OH)$][OTf]$_2$ was dissolved in 2 mL THF/DCM (1:1) and froze in a liquid nitrogen cooled cold well. 8 mg (0.03 mmol) Ph_3PCH_2 was added to the thawing solution as a THF solution. The reaction turned a deep blue, and at this point care was taken to avoid warming the mixture to room temperature. The compound was precipitated by addition of cold Et_2O, and the precipitate was dried under vacuum to yield **6** as a blue powder. NMR analysis of this powder revealed the presence of residual [Ph_3PCH_3][OTf], which were difficult to remove with Et_2O washes. This mixture could be recrystallized in THF/Et_2O at -35 °C to obtain X-ray quality crystals of **6**; however, due to the decomposition of this compound, obtaining **6** cleanly as a bulk solid for elemental analysis was unsuccessful. ^{1}H NMR (300 MHz, CD_3CN): δ 122.2 (br), 90.2 (br), 68.5, 66.1, 55.0, 53.2, 14.5, 13.9, 13.0, 10.7, -31.0 (br) ppm.

Synthesis of [$LFe_3O(PzNHtBu)_3Fe(O)$][OTf]$_2$ (7). 43.0 mg [$LFe_3O(PzNHtBu)_3Fe(OH)$][OTf]$_2$ (**3**; 0.02 mmol) was dissolved in 1:1 DCM/THF and froze in a liquid nitrogen cooled cold well. A THF solution of 6.8 mg Ph_3PCH_2 (0.02 mmol) was added to the thawing solution. The reaction

was then combined, while thawing, with a DCM solution of 7.8 mg [Fc][OTf] (0.02 mmol). Keeping this mixture as cold as possible, thawing Et_2O was added to precipitate the oxidized cluster; The blue-green solid was collected on a fine porosity glass frit, and dried under vacuum. The ^1H NMR of this solid always contained minor amounts of impurities (<20%, mostly ascribed to **3** and **4**), which **7** could not be isolated from due to its thermal instability. For any subsequent reactions performed on this material, the moles of initial cluster **3** were used to approximate the amount of **7** present. ^1H NMR (300 MHz, 1:1 CD_3CN/CD_2Cl_2): δ 145.6 (br), 105.4 (br), 85.2, 81.4, 71.0, 67.2, 19.0, 13.8, 11.1, 8.8, -61.1, -67.3 (br).

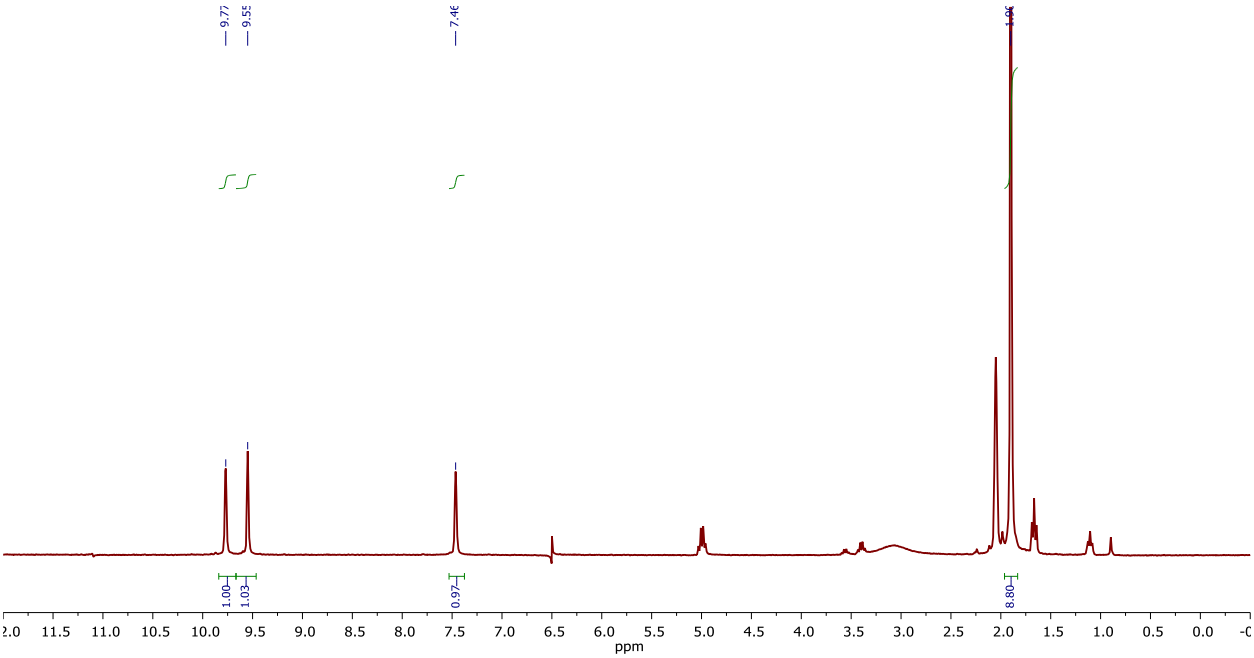

Figure S1. ^{1}H NMR spectrum (300 MHz) of 2-*tert*-butyl-isoxazolium tetrafluoroborate in $(CD_3)_2CO$.

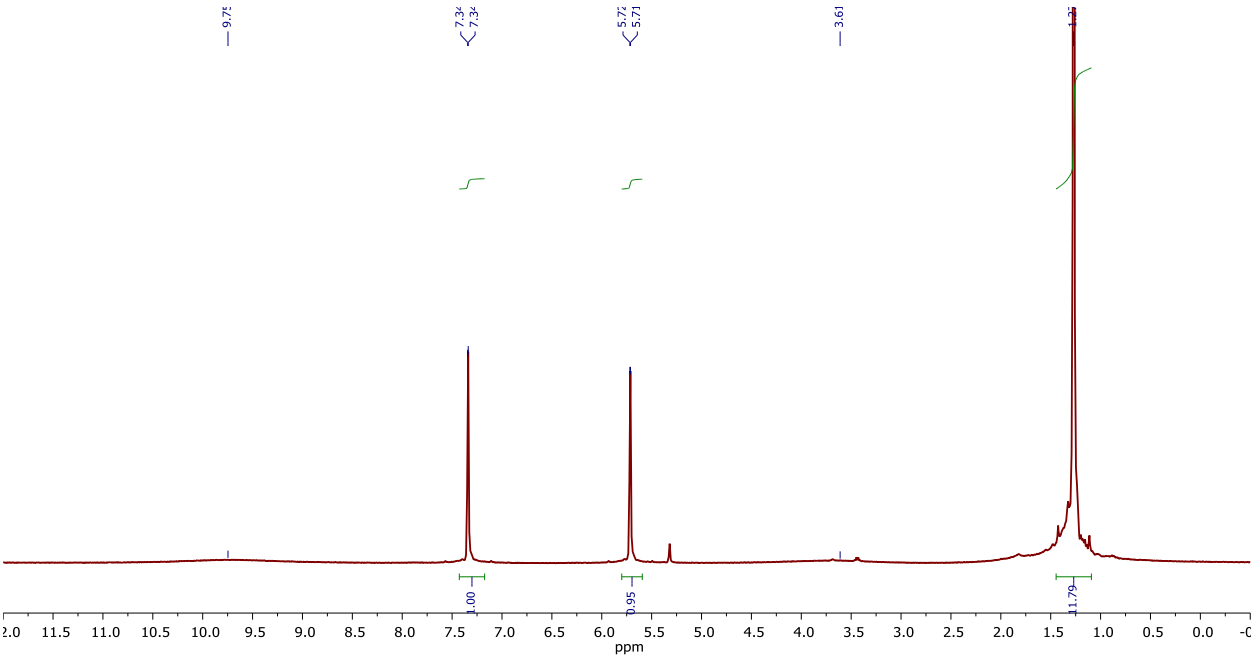

Figure S2. ^{1}H NMR spectrum (400 MHz) of *N*-*tert*-butyl-1*H*-pyrazol-3-amine in CD_2Cl_2.

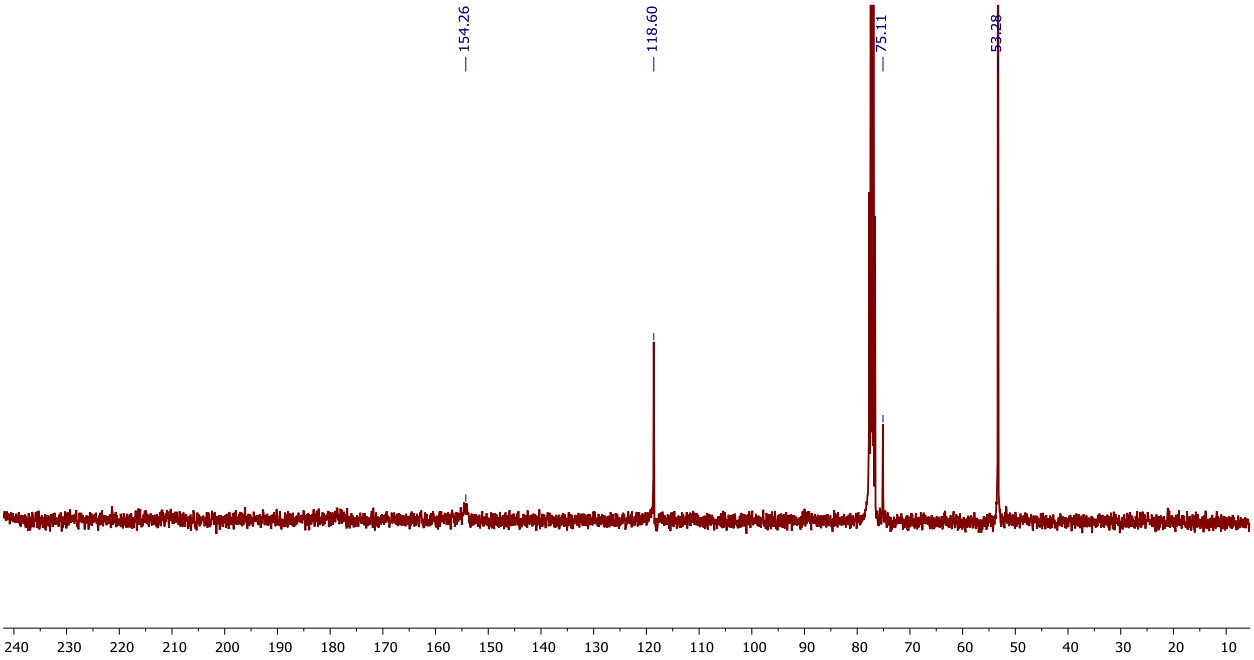

Figure S3. $^{13}C\{^{1}H\}$ NMR spectrum (100 MHz) of *N*-*tert*-butyl-1*H*-pyrazol-3-amine in CD_2Cl_2.

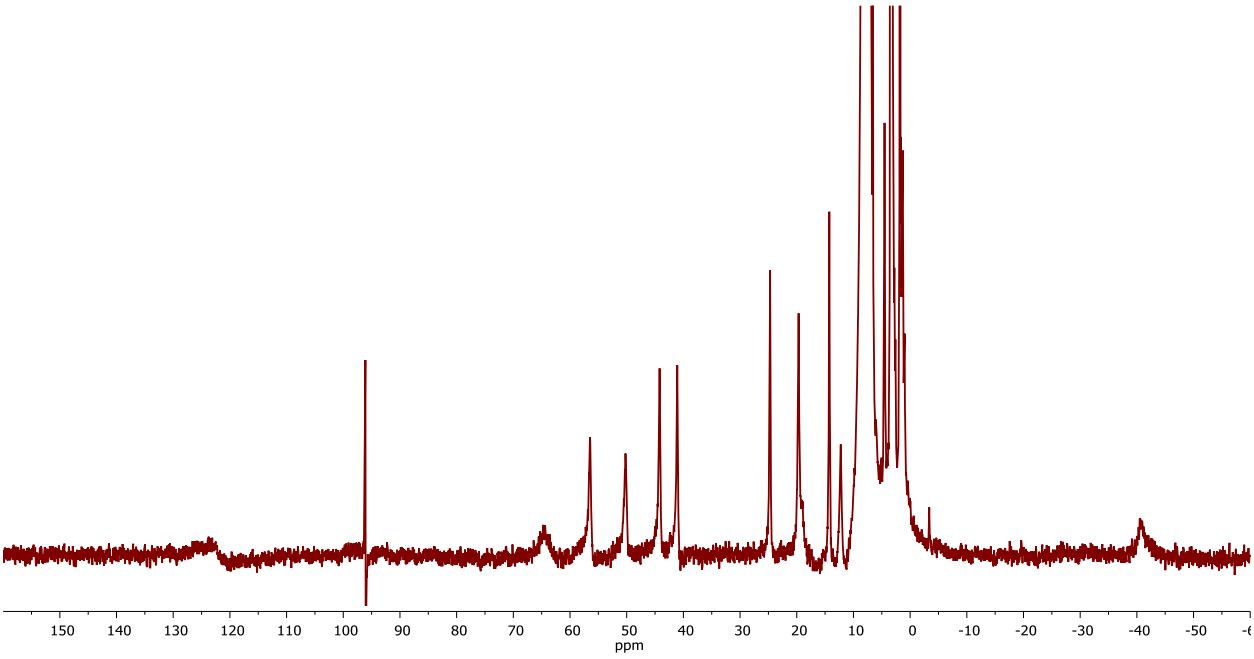

Figure S4. ^{1}H NMR spectrum (300 MHz) of $LFe_3O(PzNHtBu)_3Fe(OH)$ (**1**) in C_6D_6. The sharp signal ~ 95 ppm is a spectral artifact.

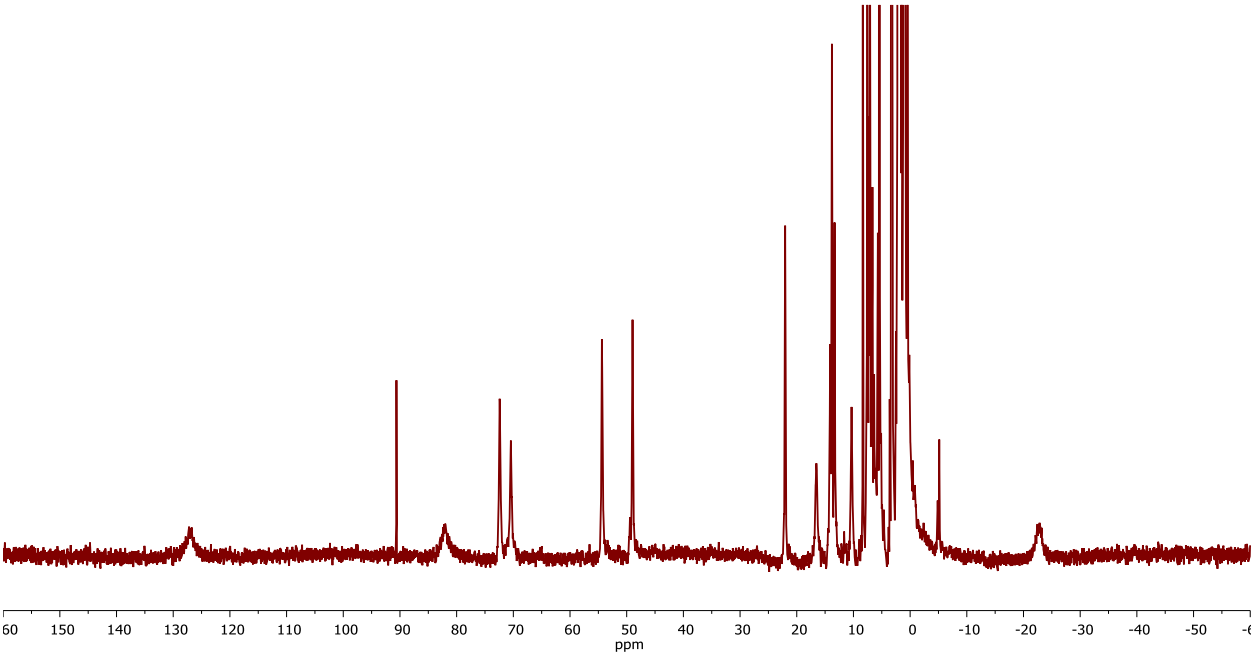

Figure S5. ^{1}H NMR spectrum (300 MHz) of [$LFe_3O(PzNHtBu)_3Fe(OH)$][OTf] (**2**) in CD_3CN. The sharp signal ~ 90 ppm is a spectral artifact.

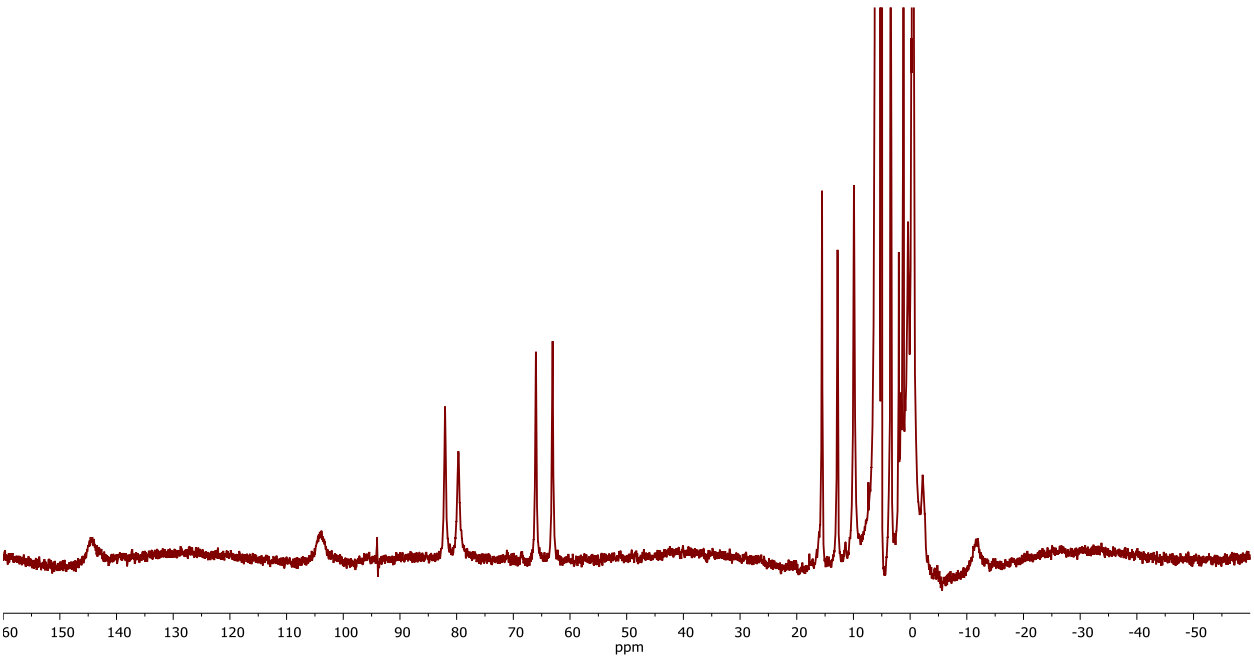

Figure S6. ^{1}H NMR spectrum (300 MHz) of [$LFe_3O(PzNHtBu)_3Fe(OH)$][OTf]$_2$ (**3**) in CD_2Cl_2.

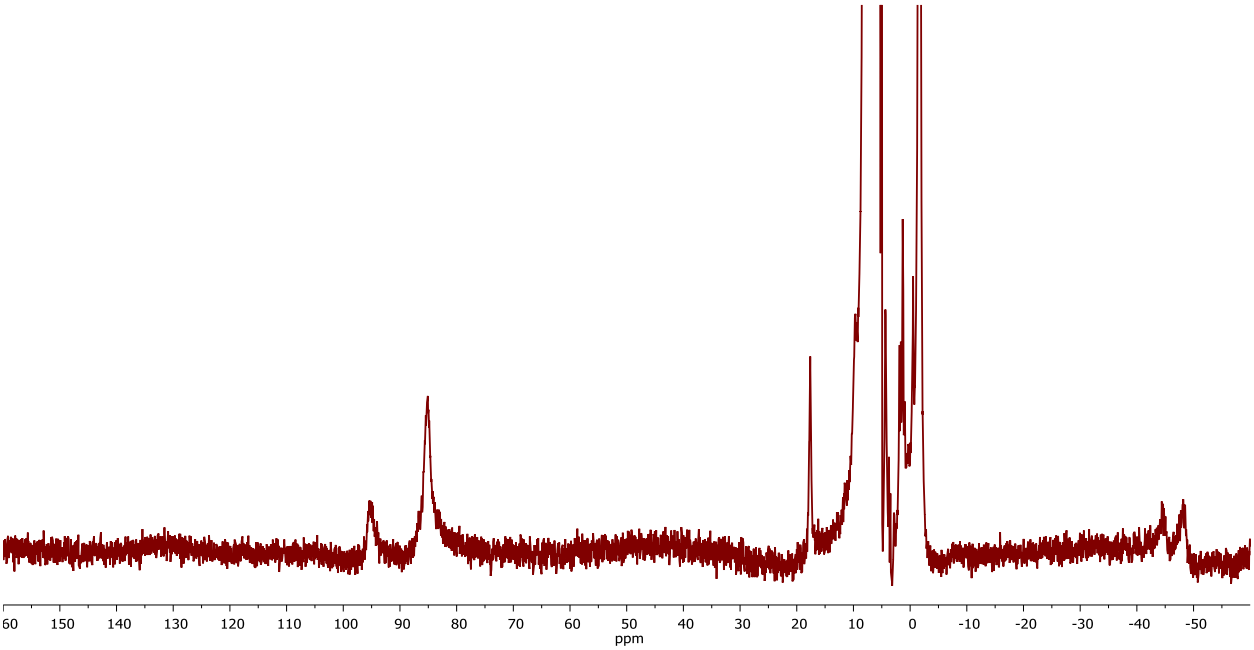

Figure S7. ^{1}H NMR spectrum (300 MHz) of [$LFe_3O(PzNHtBu)_3Fe(OH)$][$OTf]_3$ (**4**) in CD_2Cl_2.

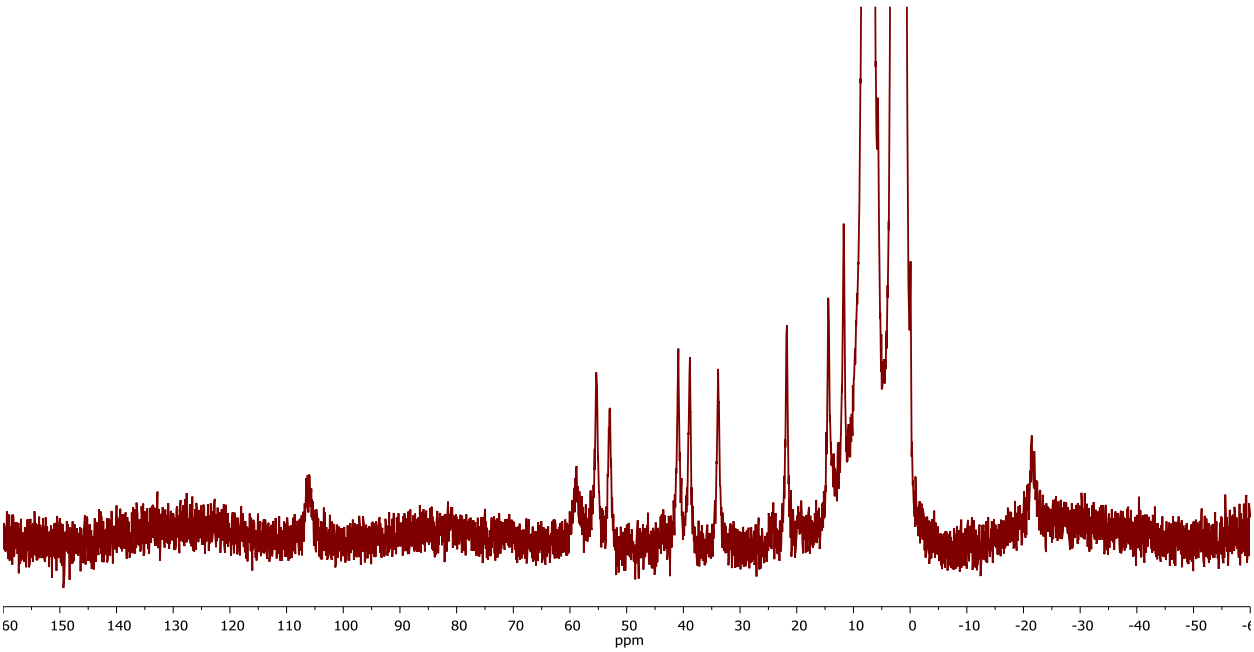

Figure S8. ^{1}H NMR spectrum (300 MHz) of $LFe_3O(PzNHtBu)_3Fe(O)$ (**5**) in C_6D_6.

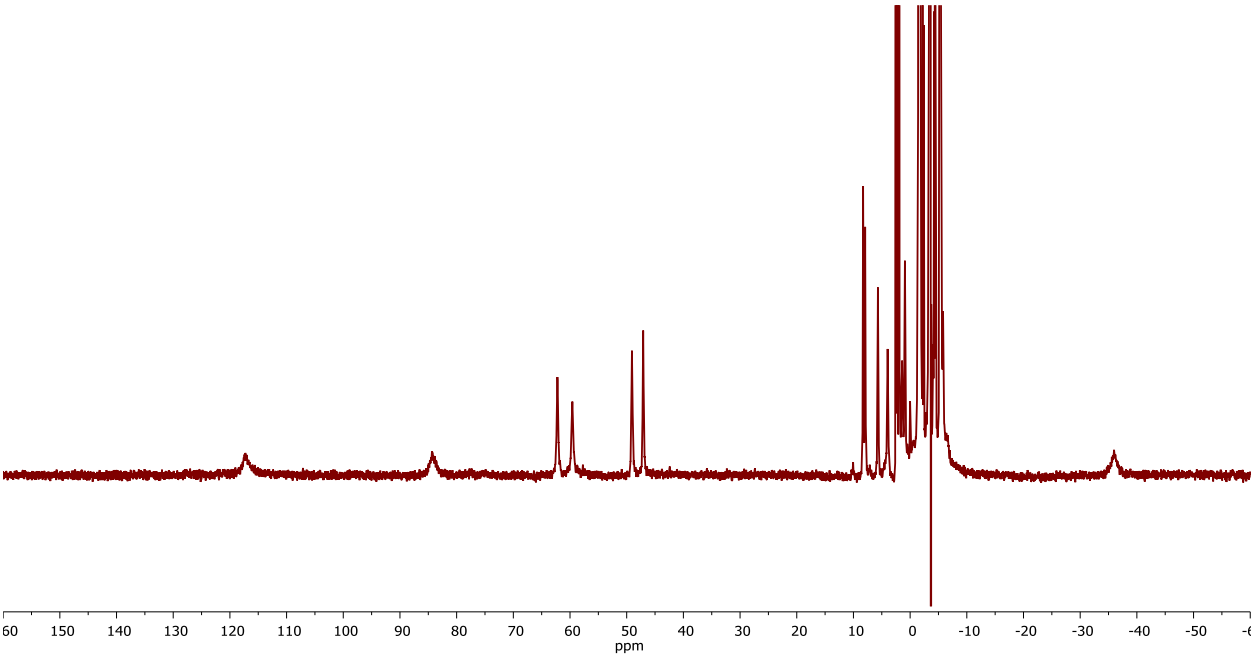

Figure S9. ^{1}H NMR spectrum (400 MHz) of [$LFe_3O(PzNHtBu)_3Fe(O)$][OTf] (**6**) in THF/C_6D_6.

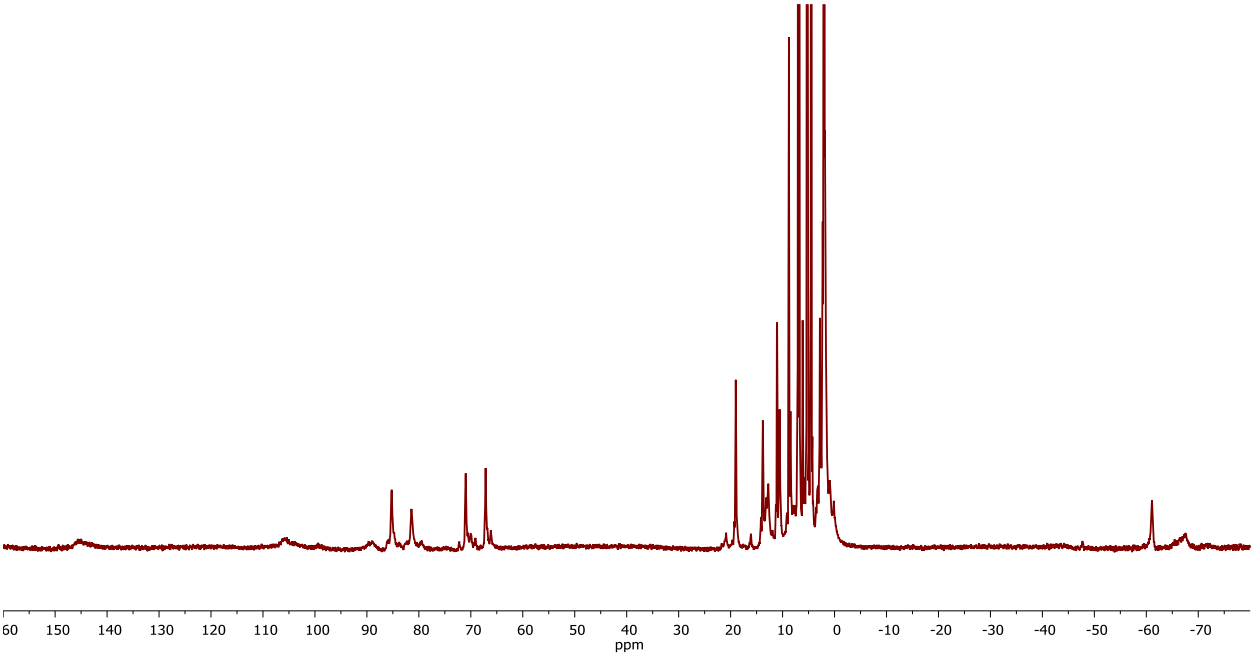

Figure S10. ^{1}H NMR spectrum (300 MHz) of [$LFe_3O(PzNHtBu)_3Fe(O)$][OTf]$_2$ (**7**) in 1:1 CD_3CN/CD_2Cl_2.

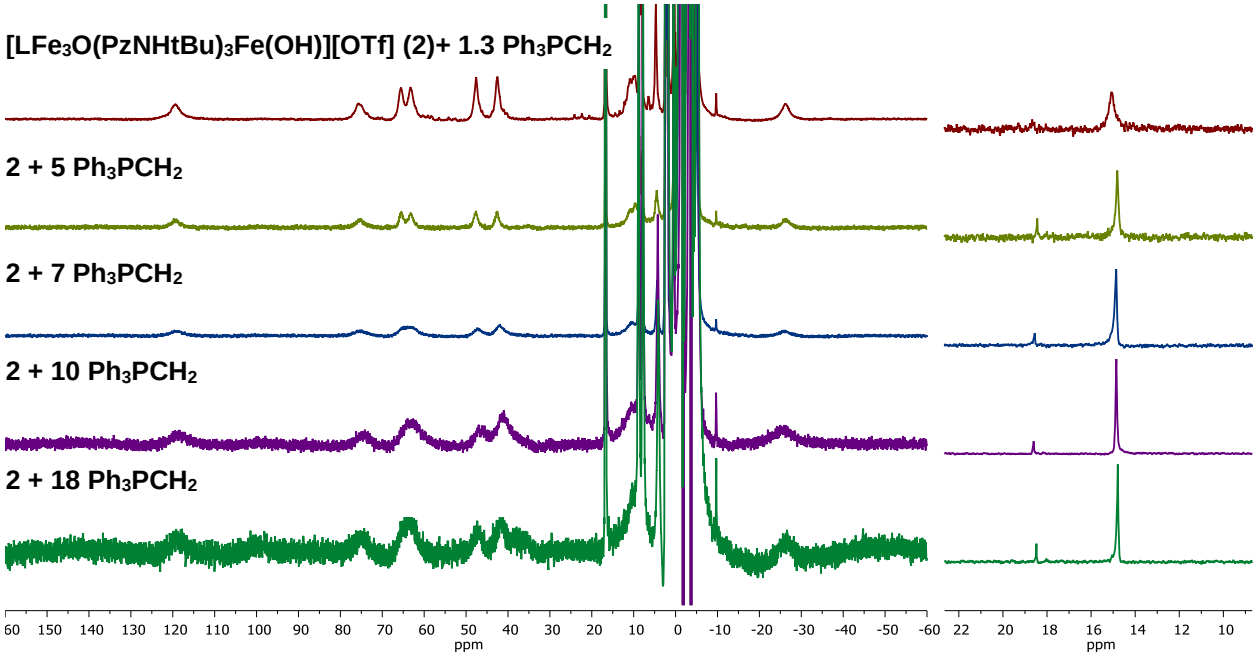

Figure S11. (Left) ^{1}H NMR spectra (400 MHz) and ^{31}P NMR spectra (120 MHz; right) of [$LFe_3O(PzNHtBu)_3Fe(OH)$][OTf] (**2**) in THF/C_6D_6 with 1.3, 5, 7, 10, and 18 equivalents Ph_3PCH_2.

NMR	Equiv. Ph_3PCH_2	Equiv. $[Ph_3PCH_2]^+$	[**5**]/[**2**]	*K*
2 + 1.3 Ph_3PCH_2	~ 1.3	-	n.d.	n.d.
2 + 5 Ph_3PCH_2	4.54	0.46	0.85	0.09
2 + 7 Ph_3PCH_2	6.38	0.62	1.63	0.16
2 + 10 Ph_3PCH_2	9.24	0.76	3.17	0.26
2 + 18 Ph_3PCH_2	16.97	1.03	n.d.	n.d.
			Average *K*	0.17 (±0.09)

Table S1. pK_a determination of [$LFe_3O(PzNHtBu)_3Fe(OH)$][OTf] (**2**) via ^{31}P NMR spectroscopy in Figure S11. Reversible deprotonation of **2** to form $LFe_3O(PzNHtBu)_3Fe(O)$ (**5**) is indicated by the broadening of the paramagnetically shifted peaks in the ^{1}H NMR. The ratio of **2** to **5** was estimated from the relative integrals of the ^{31}P NMR peaks for Ph_3PCH_2 (~15 ppm) and $Ph_3PCH_3^+$ (~18 ppm); it was assumed that the equivalents of $[Ph_3PCH_3]^+$ produced in the NMR were due to partial deprotonation of **2**, and corresponded to equivalents of **5** ([$[Ph_3PCH_3][OTf]$] = [**5**]). An equilibrium constant was determined according to the equation below:

$$K = \frac{[\mathbf{5}]\left[[Ph_3PCH_3][OTf]\right]}{[\mathbf{2}][Ph_3PCH_2]}$$

This value, along with the reported pK_a of Ph_3PCH_2 in THF, 29.3, was used to obtain a pK_a value of 30.1 (±1.0) for **2**.[8]

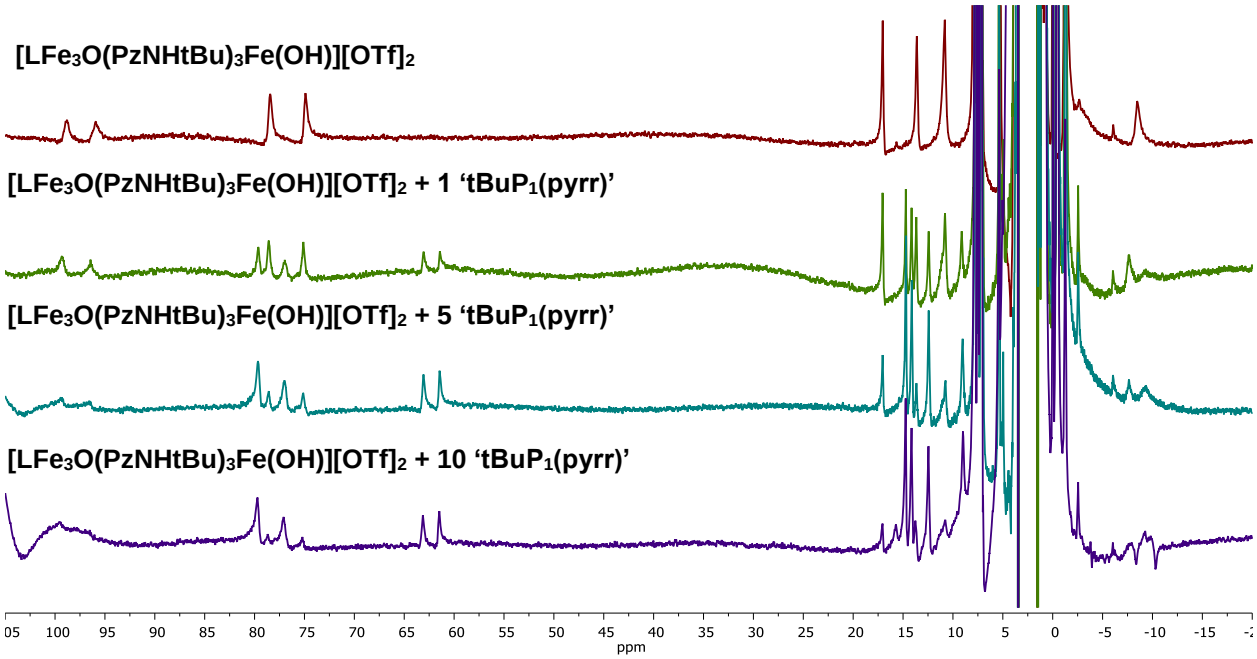

Figure S12. ^{1}H NMR spectra (400 MHz) of [LFe$_3$O(PzNHtBu)$_3$Fe(OH)][OTf]$_2$ (**3**) in THF/C$_6$D$_6$ with 1, 5, and 10 equivalents *tert*-butylimino-tri(pyrrolidino)phosphorene ('tBuP$_1$(pyrr)') at -20 °C.

NMR	Equiv. **3**	Equiv. **6**	*K*
3 + 1 tBuP$_1$(pyrr)	0.55	0.45	0.70
3 + 5 tBuP$_1$(pyrr)	0.27	0.73	0.46
3 + 10 tBuP$_1$(pyrr)	0.12	0.88	0.71
		Average *K*	0.62 (±0.14)

Table S2. pK_a determination of **3** via ^{1}H NMR spectroscopy in Figure S12. The equilibrium of **3** and **6** is slow, relative to the NMR timescale. The ratio of **3** to **6** was based on the relative integrals of the ^{1}H NMR peaks at 17.0 (for **3**) and 14.5 ppm (for **6**); the relative amounts of base and conjugate acid of 'tBuP$_1$(pyrr)' were assumed based on mass balance. An equilibrium constant was determined according to the equation below:

$$K = \frac{[\mathbf{6}]\left[['\mathrm{HtBuP_1(pyrr)'}][\mathrm{OTf}]\right]}{[\mathbf{3}]['\mathrm{tBuP_1(pyrr)'}]}$$

This value, along with the reported pK_a of 'tBuP$_1$(pyrr)' in THF, 22.8, was used to obtain a pK_a value of 23.0 (±1.0) for **3**.[8]

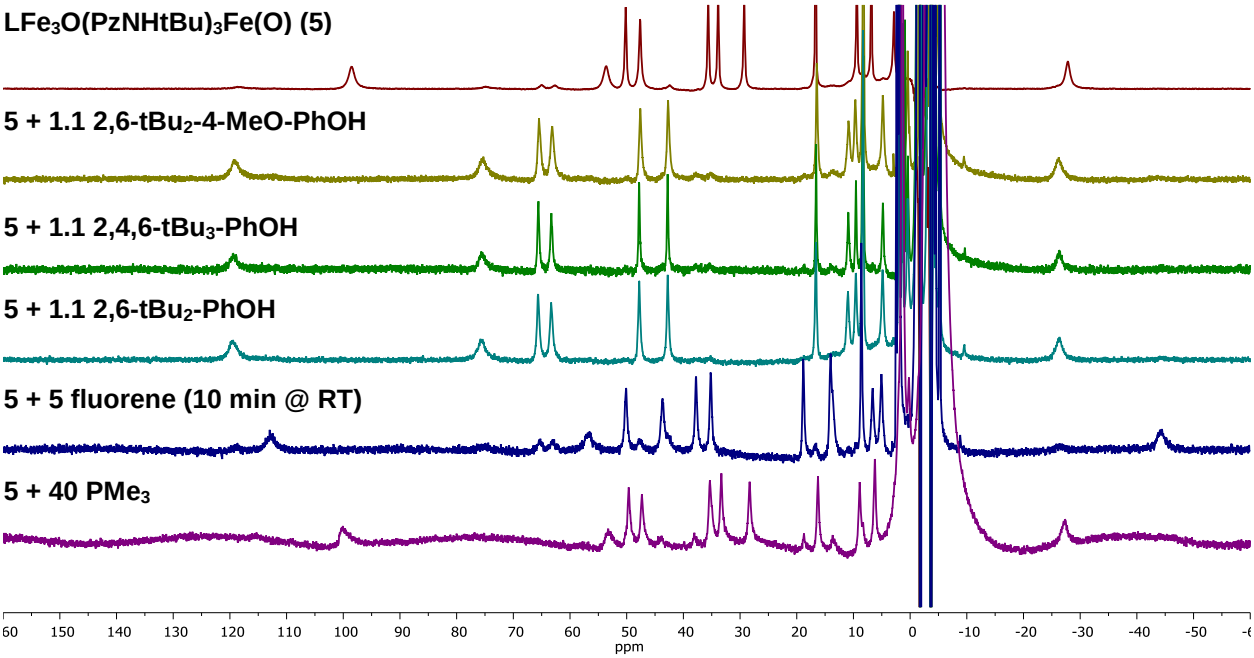

Figure S13. ^{1}H NMR spectra (400 MHz) in THF/C_6D_6 of reaction products with $LFe_3O(PzNHtBu)_3Fe(O)$ (**5**) and substituted phenols, 5 equivalents fluorene, and 40 equivalents trimethylphospine. The ^{1}H NMRs of the reactions with phenols are identical to the NMR of $[LFe_3O(PzNHtBu)_3Fe(OH)][OTf]$ (**2**). The major product in the reaction with fluorene matches the ^{1}H NMR spectrum of $LFe_3O(PzNHtBu)_3Fe(OH)$ (**1**).

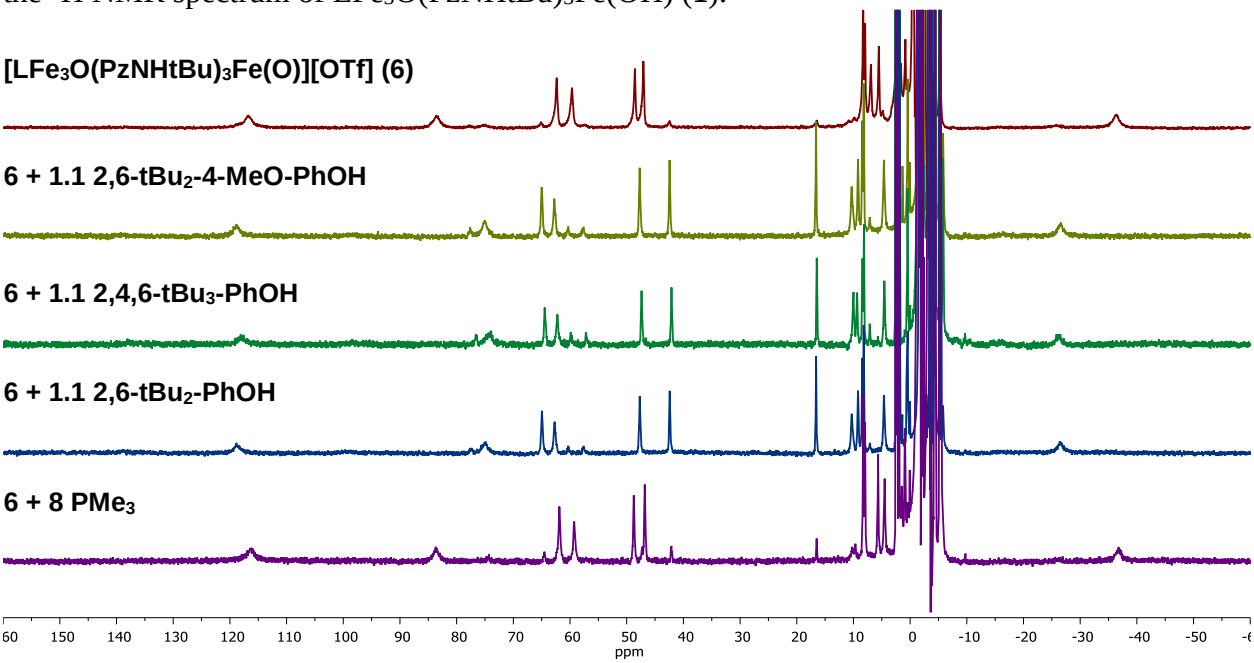

Figure S14. ^{1}H NMR spectra (400 MHz) in THF/C_6D_6, with 1 – 2 equivalents of $[^{n}Pr_4N][BAr^{F}_4]$, of reaction products of $[LFe_3O(PzNHtBu)_3Fe(O)][OTf]$ (**6**) with substituted phenols, and 8 equivalents trimethylphospine. The major product of the reactions with phenols matches the NMR spectrum of $[LFe_3O(PzNHtBu)_3Fe(OH)][OTf]$ (**2**).

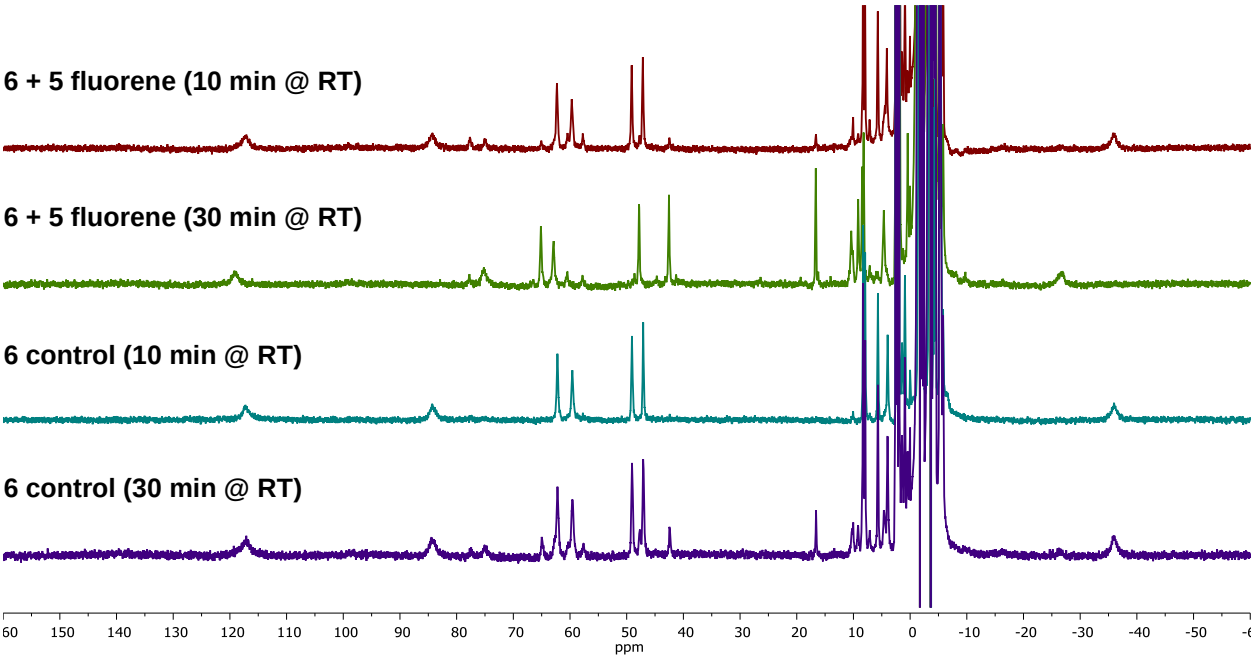

Figure S15. ^{1}H NMR spectra (400 MHz) in THF/C_6D_6, with 1 equivalent of [$^{n}Pr_4N$][BAr^{F}_4], of reaction product of [$LFe_3O(PzNHtBu)_3Fe(O)$][OTf] (**6**) with 5 equivalents of fluorene, at 10 and 30 minutes. The major product of the reaction after 30 minutes matches the NMR spectrum of [$LFe_3O(PzNHtBu)_3Fe(OH)$][OTf] (**2**).

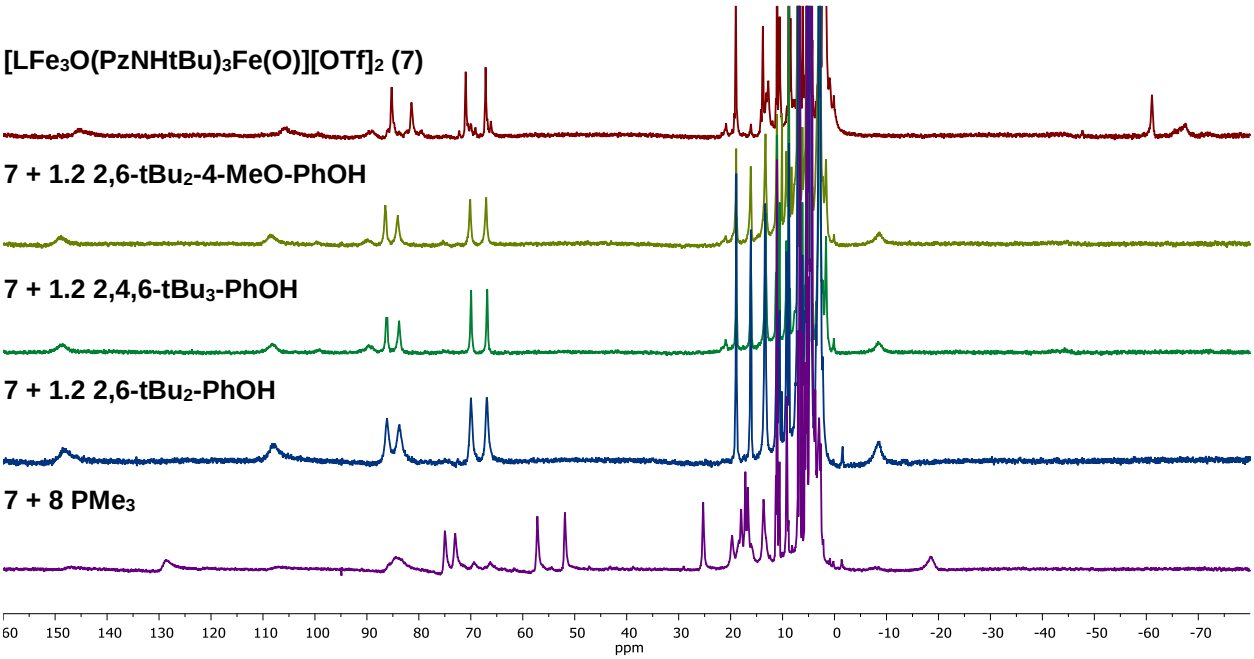

Figure S16. ^{1}H NMR spectra (300 MHz) in 1:1 CD_3CN/CD_2Cl_2, of reaction product of [$LFe_3O(PzNHtBu)_3Fe(O)$][OTf]$_2$ (**7**) with substituted phenols and 8 equivalents trimethylphosphine. The major product of the reactions with phenols matches the NMR spectrum of [$LFe_3O(PzNHtBu)_3Fe(OH)$][OTf]$_2$ (**3**).

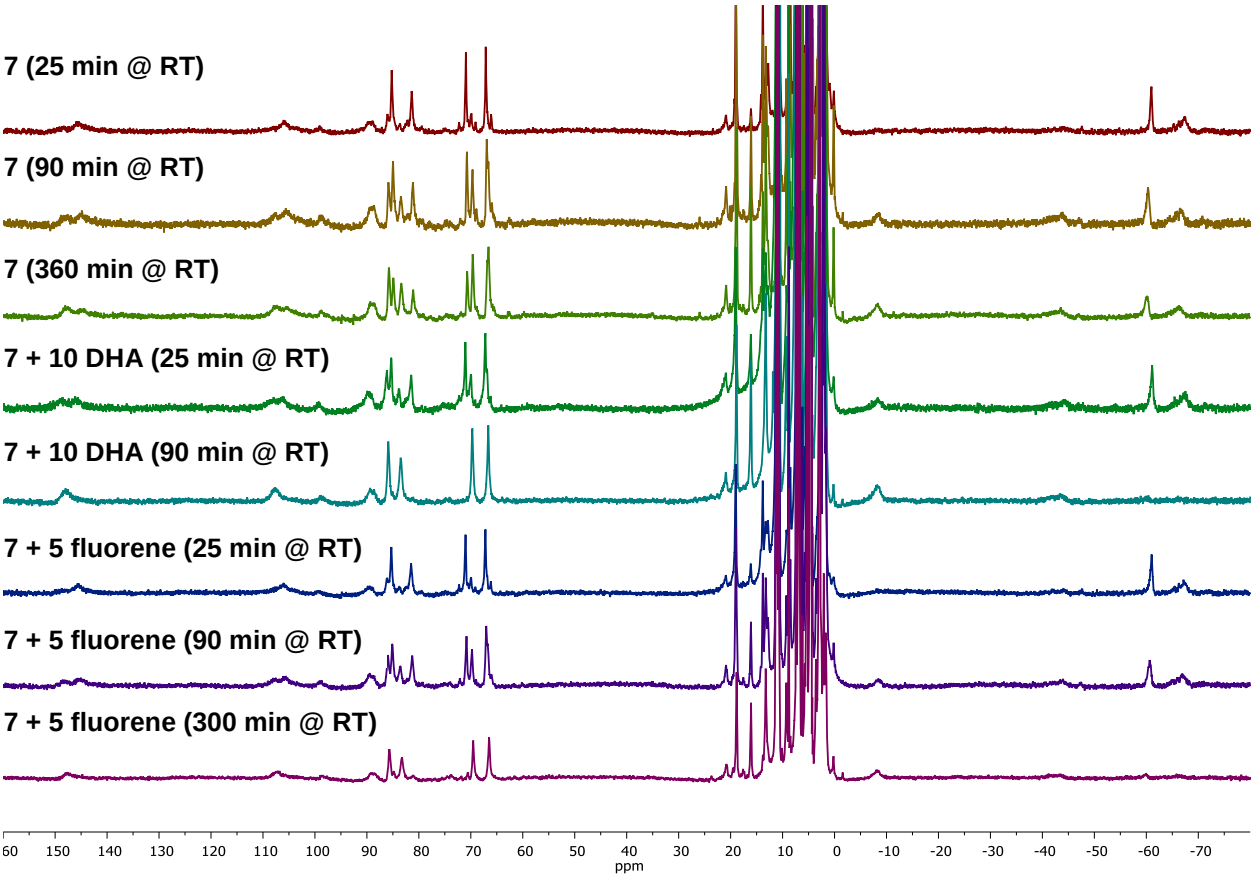

Figure S17. ^{1}H NMR spectra (300 MHz) in 1:1 CD_3CN/CD_2Cl_2, of reaction product of $[LFe_3O(PzNHtBu)_3Fe(O)][OTf]_2$ (**7**) with 9,10-dihydroanthracene and fluorene. By itself, **7** decays significantly over 6 hours, but it is present in ~40%, relative to its decomposition products (**3** and **4**). In the presence of DHA, conversion to mostly **3** occurs over 90 minutes; likewise, **7** reacts with fluorene but on a timescale closer to its background decomposition (complete after 5 hours).

Product analysis of oxidation reactions between 5 – 7 and 9,10-dihydroanthracene, fluorene, and 2,4,6-tri-tert-butylphenol: 2mM solutions of Fe-oxo clusters **5** – **7** were stirred for 12-24 hours with one equivalent of 9,10-dihydroanthracene (DHA) or fluorene. The solvent was removed under vacuum and the organic products were extracted with Et_2O containing triphenylphosphine as an internal standard. The suspensions were filtered over celite and analyzed via GC-MS. The oxidized products (anthracene and 9,9'-bifluorene) were quantified based on a calibration curve of authentic samples. Other possible oxidation products, such as fluorenone, or anthraquinone, were not observed. Yields reported as percentage based on a 2:1 cluster-substrate stoichiometry. For the reactions with fluorene, no 9,9'-bifluorene was observed, except in trace amounts with **6**; due to the noticeable rates of reaction with compounds **5** -**7** by ^{1}H NMR (Figures S13, S15, and S17), and high yield of the corresponding Fe-hydroxide clusters, we postulate that PCET reactions with fluorene occur, but potentially produces multiple oxidized organic products.

Conversion of the Fe-oxo cluster to the corresponding reduced Fe-hydroxide cluster following reactions with DHA and fluorene was measured by collecting an NMR of the metal complexes with a 1,4-bis-trimethylsilyl-benzene internal standard; yields are based on integrations of authentic samples of the Fe-hydroxide clusters **1** – **3**. An EPR spectrum of **6** and 2,4,6-tri-tertbutylphenol was collected in 2-methyl tetrahydrofuran at 77 K and a signal for the corresponding phenoxyl radical was observed, supporting a PCET process.

Assignment of the reaction as PT or PCET was made based on the cluster products, since these compounds can be clearly identified by ^{1}H NMR, in all cases.

	5		**6**		**7**	
Substrate	organic product	cluster product	organic product	cluster product	organic product	cluster product
9,10 -dihydroanthracene	anthracene (53%)	**1** (67%)	anthracene (43%)	**2** (66%)	anthracene (44%)	**3** (110%)
fluorene	n.d.	**1** (83%)	9,9'-bifluorenyl (1%)	**2** (81%)	n.d.	**3** (107%)
2,4,6-tri-tertbutylphenol	-	**2**	phenoxyl radical	**2**	-	**3**
trimethylphosphine	N.R.	N.R.	N.R.	N.R.	$OPMe_3$	**2**

Table S3. Yields of PCET reactions between 9,10-dihydroanthracene, fluorene, or 2,4,6-tri-tertbutylphenol with the Fe-oxo clusters **5** – **7**.

18-Oxygen incorporation into the *tert*-butyl amino pyrazolate bridged tetranuclear Fe clusters: ESI-MS analysis of clusters prepared with $K^{18}OH$ show ion peaks consistent with 18-O incorporation (**A**-**D** + 2 m/z). However, observation of **A** + 2 m/z is most consistent with ^{18}O-incorporation at the μ_4-oxo position (no hydroxide bound to apical Fe). We postulate that exchange with adventitious H_2O leads to loss of ^{18}O label at hydroxide during the ESI-MS measurement (which was done under air); support for this idea is the observation of a marginally higher m/z + 2 parent ion peak (**C** in **2-^{18}O**), which could be assigned to un-exchanged $LFe_3{}^{18}O(PzNHtBu)_3Fe(^{18}OH)^+$. It also seems unlikely that the excess (~ 8 equiv.) $K^{18}OH$ would only selectively incorporate into the bridging oxo position.

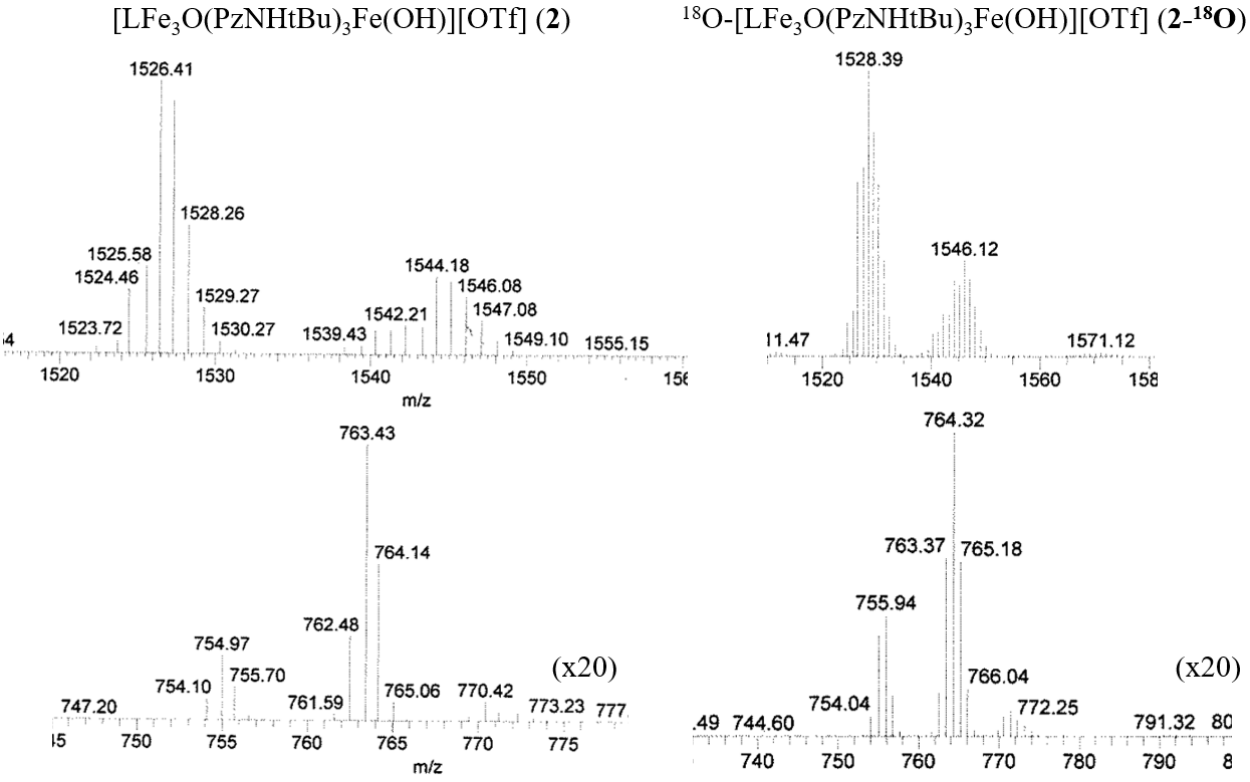

Ion	m/z (calc.)
$LFe_3O(PzNHtBu)_3Fe^{2+}$ (**A**)	754.7
$LFe_3O(PzNHtBu)_3Fe(OH)^{2+}$ (**B**)	763.2
$LFe_3O(PzNHtBu)_3Fe(OH)^+$ (**C**)	1526.4
$LFe_3O(PzNHtBu)_3Fe(OH)^+ + H_2O$ (**D**)	1544.4
$LFe_3O(PzNHtBu)_3Fe(Cl)^+$ (**E**)	1544.3

Figure S18. ESI-MS spectra of **2** from **1** produced from natural abundance KOH (left) or $K^{18}OH$ (right). The chart lists ion assignments based on natural abundance oxygen, with the calculated mass to charge ratio (m/z).

Oxygen atom transfer studies of oxidized Fe_4-oxo cluster with trimethylphosphine: The ^{18}O-[Fe^{III}_4]-oxo cluster was prepared in situ by combining a thawing 1:1 THF/DCM solution of 50.3 mg ^{18}O-[$LFe_3O(PzNHtBu)_3Fe(OH)$][OTf]$_2$ (**3-^{18}O**; 0.03 mmol) with 7.5 mg Ph_3PCH_2 (0.03 mmol) to prepare a solution of ^{18}O-[$LFe_3O(PzNHtBu)_3Fe(O)$][OTf] (**6-^{18}O**). This solution was combined, while thawing, to a DCM solution of 9.5 mg [Fc][OTf] (0.03 mmol). Keeping this mixture as cold as possible, thawing Et_2O was added to precipitate the oxidized cluster; boron nitride (BN) was added to ease separation of precipitate from the solution. This suspension was filtered to obtain solid **^{18}O-7**, which was eluted from BN with cold 1:1 THF/DCM. 50 μL PMe_3 (0.50 mmol) was added to solution as it thawed, and was gradually warmed to room temperature. ^{31}P NMR analysis of the reaction mixture at this stage showed a peak consistent with trimethylphosphine oxide ($OPMe_3$) formation at ~35 ppm. (^{1}H NMR spectra of these reactions only displayed paramagnetic peaks characteristic of reduced [Fe_4]-hydroxide clusters, **2** and/or **3**, which we ascribe to a cluster decomposition reaction, where the resulting [$Fe^{II}_2Fe^{III}_2$] cluster formed after oxygen atom transfer to PMe_3 is unstable and must decompose in some fashion which precludes observation of any sharp paramagnetic peaks in the NMR.) After 30 minutes, the reaction was pumped down. On the bench, the crude reaction mixture was separated via silica plug; 10% MeOH in DCM was used to elute a dark solution, at which point MeOH was washed through the plug to collect a fraction containing $OPMe_3$. The MeOH fraction was pumped down and analyzed via GC/MS, which displayed a GC peak characteristic of $OPMe_3$, with both $^{16}OPMe_3$ and $^{18}OPMe_3$ based on its mass spectrum.

These observations demonstrate that an oxygen atom is transferred from the tetranuclear cluster to PMe_3, albeit in low yields, and with no observation of the postulated vacant [$Fe^{II}_2Fe^{III}_2$] cluster. Recently, we have reported oxygen atom transfer to phosphines from related multinuclear Fe and Mn clusters, bearing μ_2-OH and/or $\mu_{3\geq}$-O moieties.[9] Therefore, it is possible the reactivity we observe here is between PMe_3 and the μ_4-O; although, the apparent rate of reaction here is much faster than that observed for the related Fe clusters (24+ hr to completion), which suggests the oxygen atom transfer occurs with an oxygen ligand other than the μ_4-O.

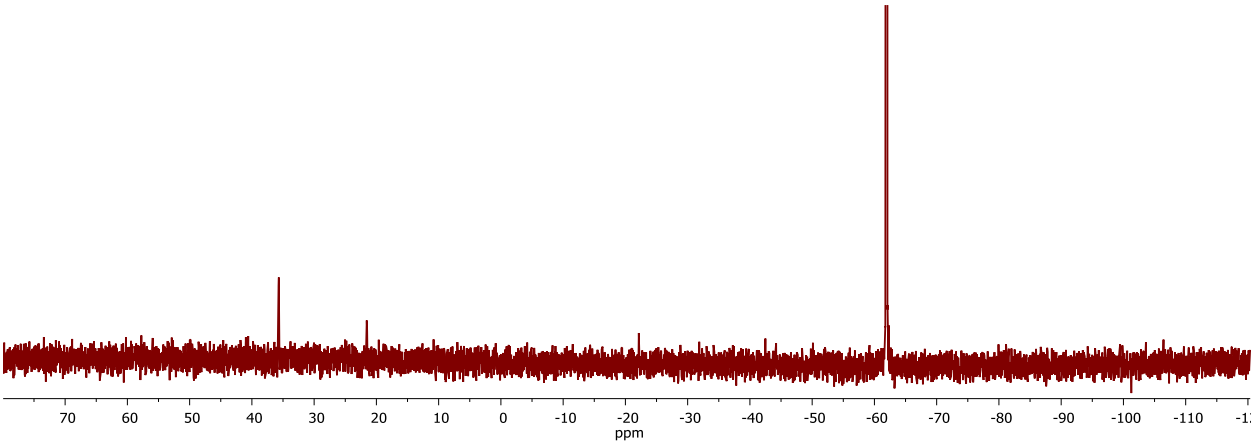

Figure S19. ^{31}P NMR spectra (120 MHz; right) of [$LFe_3O(PzNHtBu)_3Fe(O)$][OTf] (**6**) with [Fc][OTf] and 20 equivalents PMe_3.

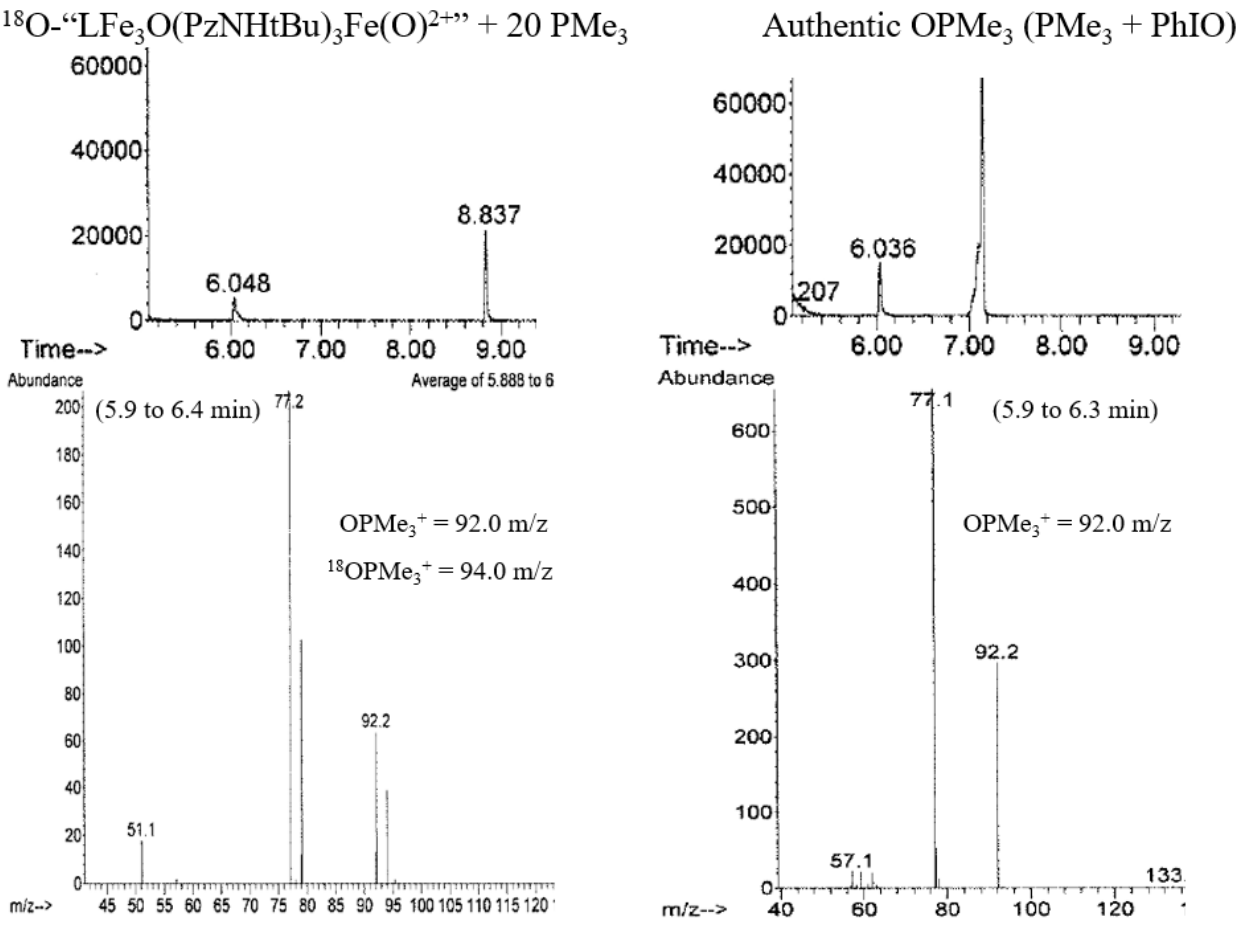

Figure S20. GC/MS chromatographs of the reaction between ^{18}O-"LFe$_3$OPzNHtBu)$_3$Fe(O)$^{2+}$" (preparation described above) and PMe$_3$ (left) and independently prepared OPMe$_3$ by addition of PMe$_3$ to a suspension of PhIO (right).

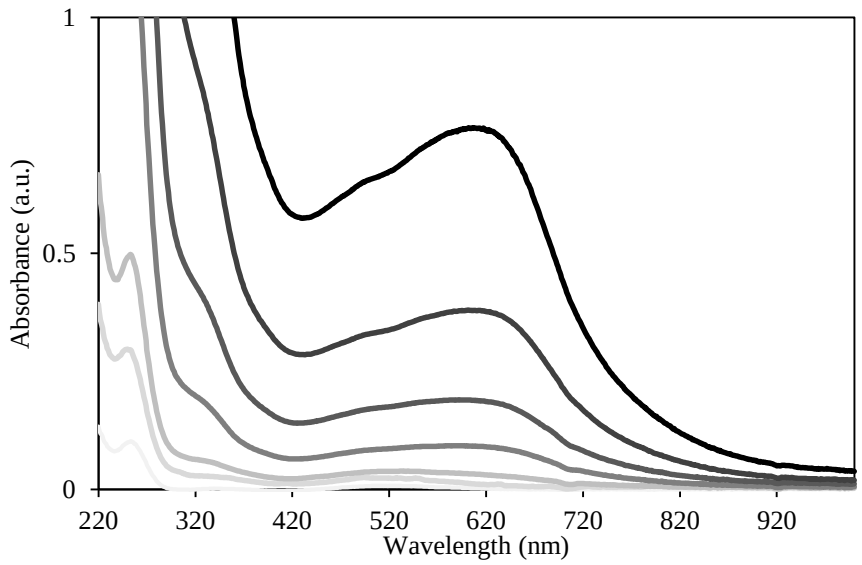

Figure S21. UV-Vis absorbance spectra of $LFe_3O(PzNHtBu)_3Fe(OH)$, **1** (1 cm cuvette; 200, 100, 50, 25, 10, 5, and 2.5 μM) in THF. [ε (M^{-1} cm^{-1})] 253 nm (5.19 x 10^4), 494 nm (3.26 x 10^3), 609 nm (3.81 x 10^3).

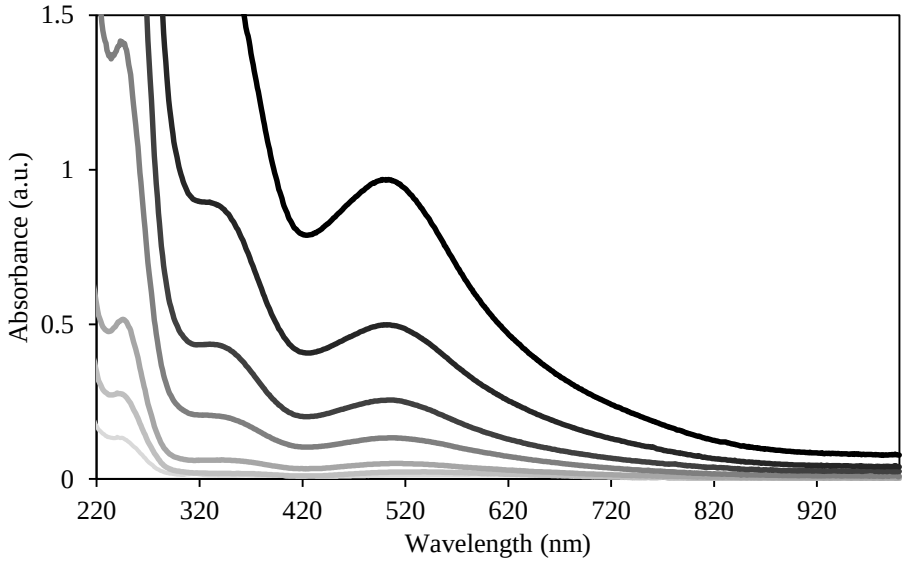

Figure S22. UV-Vis absorbance spectra of $[LFe_3O(PzNHtBu)_3Fe(OH)][OTf]$, **2** (1 cm cuvette; 200, 100, 50, 25, 10, 5, and 2.5 μM) in MeCN. [ε (M^{-1} cm^{-1})] 243 nm (5.96 x 10^4), 328 nm (8.83 x 10^3), 503 nm (4.88 x 10^3).

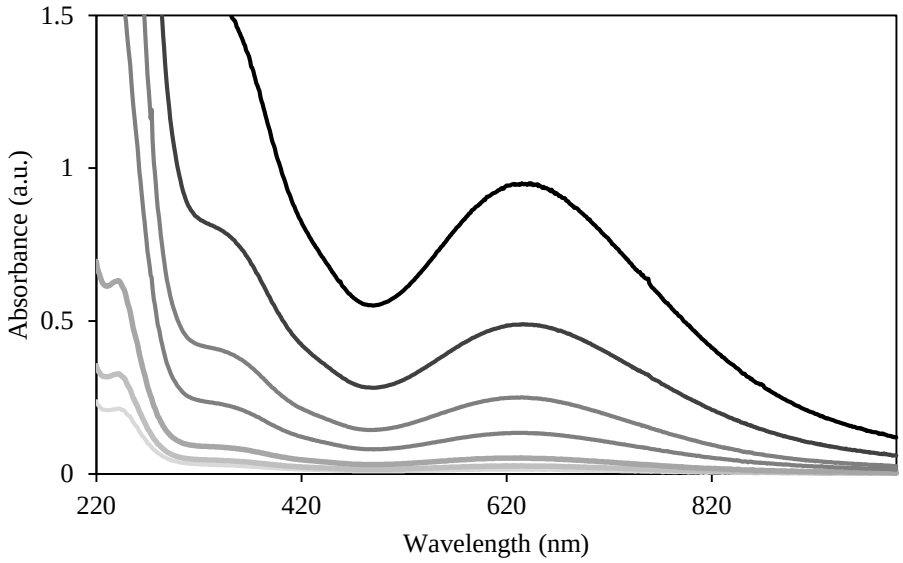

Figure S23. UV-Vis absorbance spectra of $[LFe_3O(PzNHtBu)_3Fe(OH)][OTf]_2$, **3** (1 cm cuvette; 200, 100, 50, 25, 10, 5, and 2.5 μM) in MeCN. [ε (M^{-1} cm^{-1})] 238 nm (5.76 x 10^4), 345 nm (7.74 x 10^3), 634 nm (4.80 x 10^3).

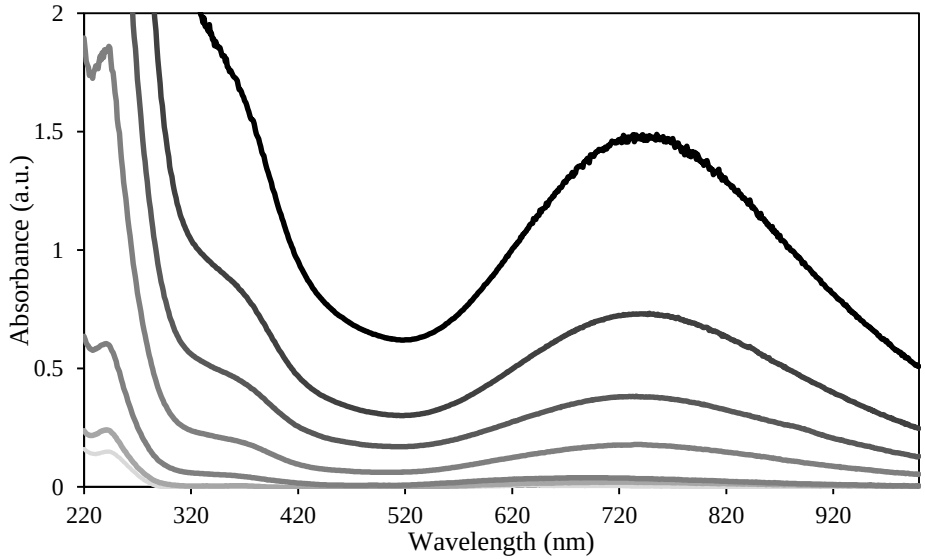

Figure S24. UV-Vis absorbance spectra of $[LFe_3O(PzNHtBu)_3Fe(OH)][OTf]_3$, **4** (1 cm cuvette; 200, 100, 50, 25, 10, 5, and 2.5 μM) in MeCN. [ε (M^{-1} cm^{-1})] 242 nm (7.11 x 10^4), 355 nm (8.85 x 10^3), 748 nm (7.39 x 10^3).

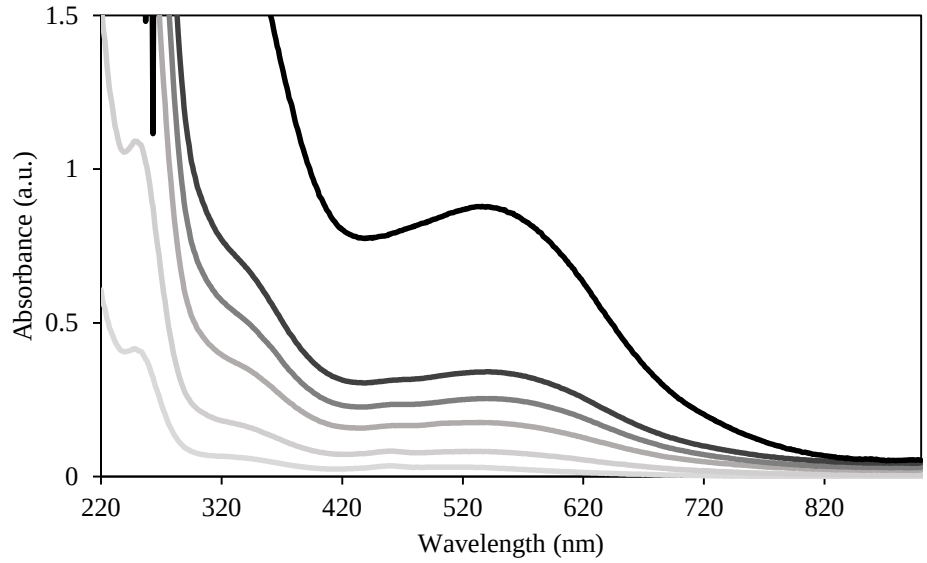

Figure S25. UV-Vis absorbance spectra of $LFe_3O(PzNHtBu)_3Fe(O)$, **5** (1 cm cuvette; 200, 100, 75, 50, 25, 10 μM) in THF. [ε (M^{-1} cm^{-1})] 248 nm (4.40 x 10^4), 342 nm (6.73 x 10^3), 539 nm (3.41 x 10^3).

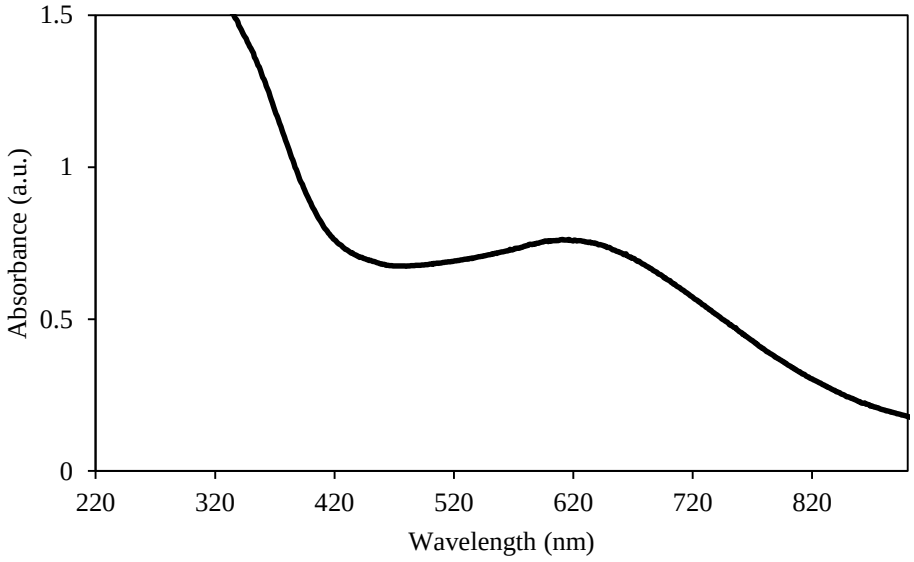

Figure S26. UV-Vis absorbance spectrum of $[LFe_3O(PzNHtBu)_3Fe(O)][OTf]$, **6** (1 cm cuvette; 200 μM) in MeCN.

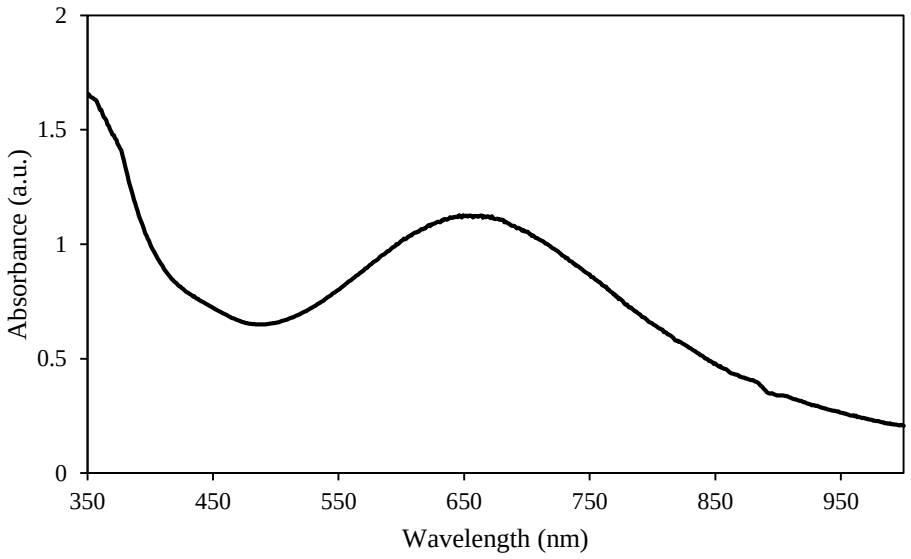

Figure S27. UV-Vis absorbance spectrum of $[LFe_3O(PzNHtBu)_3Fe(O)][OTf]_2$, **7** (1 cm cuvette; 200 μM) in MeCN.

Substrate	BDE (kcal/mol)[10]	pK_a (DMSO)	k_2 (M^{-1} s^{-1}) with **5**
xanthene	75.2	30.0[11]	40
1,4-cyclohexadiene	76.0	~34[a]	~0.3
9,10-dihydroanthracene	76.3	30.1[11]	87
triphenylmethane	81.0	30.6[12]	~0.7
fluorene	82.2	22.6[12]	~3 x 10^6

Table S4. Reported bond dissociation enthalpies (in kcal mol^{-1}) and pK_a values (in DMSO) of various organic substrates investigated for PCET reactivity with $LFe_3O(PzNHtBu)_3Fe(O)$ (**5**), with their measured second order rate constants. ^{1}H NMR analysis of the reaction mixtures after kinetics measurements show formation of **1** in all cases, consistent with a PCET process.

[a]A reported pK_a value for 1,4-cyclohexadiene could not be obtained, but is approximated based on the reported pK_a value of 1,3-cyclohexadiene in DMSO (pK_a(1,3) = 35.0) and the energy of isomerization between 1,3-cyclohexadiene and 1,4-cyclohexadiene (-1.6 kcal/mol):[13]

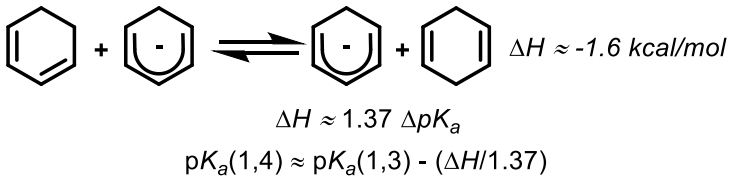

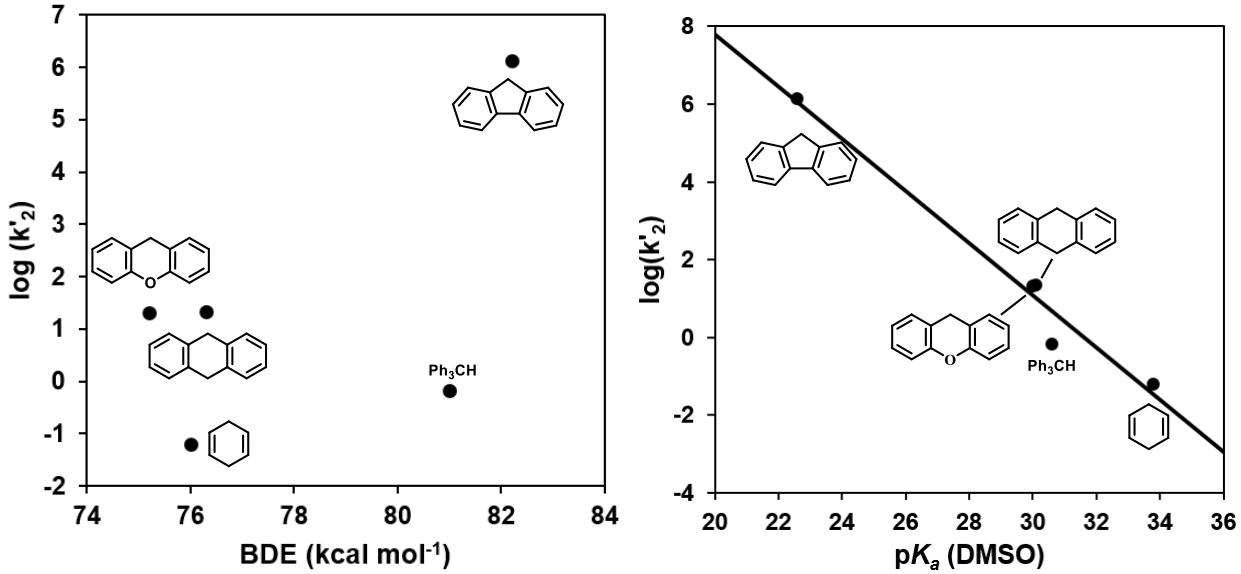

Figure S28. Plots of log (k_2) (normalized to number of reactive C-H bonds) versus BDE (left) and pK_a (in DMSO; right) for **5** with various organic substrates. The linear trend of reaction rate with pK_a of the C–H bonds is consistent with a basicity-driven mechanism of PCET for **5**.

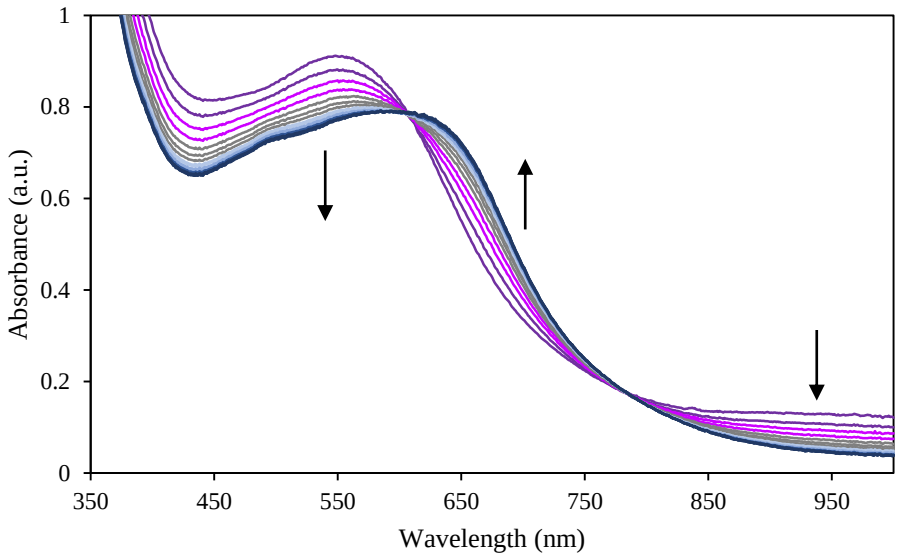

Figure S29. UV-Vis absorbance spectra of $LFe_3O(PzNHtBu)_3Fe(O)$ (**5**; 200 μM) and xanthene (10 mM) at ambient temperature.

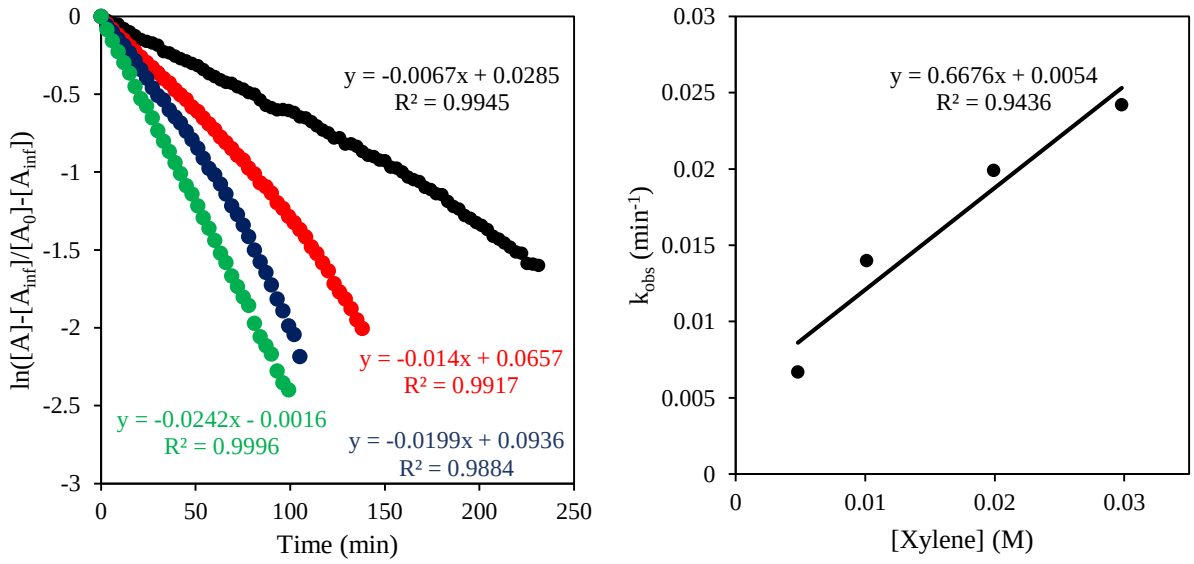

Figure S30. Kinetics data for the reaction between $LFe_3O(PzNHtBu)_3Fe(O)$ (**5**; 200 μM) and xanthene (4.8, 10.1, 19.9, and 29.8 mM) at ambient temperature. The decay of the UV-Vis absorbance feature at 540 nm was used to follow the reaction.

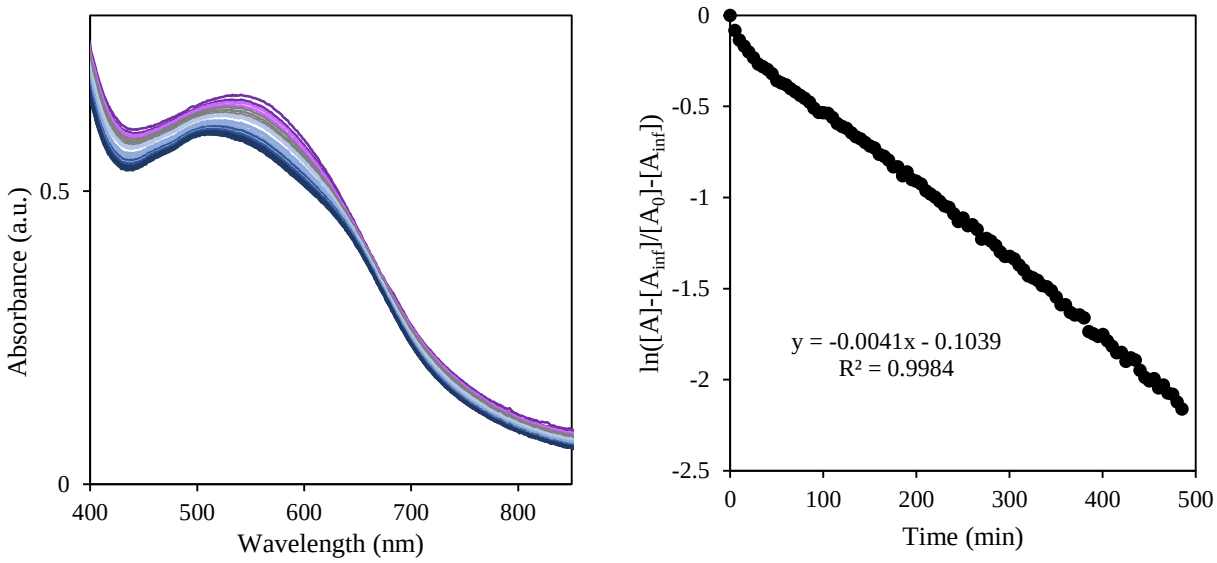

Figure S31. (Left) UV-Vis absorbance spectra of $LFe_3O(PzNHtBu)_3Fe(O)$ (**5**; 200 μM) and 1,4-cyclohexadiene (1 M) at ambient temperature. (Right) Pseudo-first order kinetics plot of the reaction by following the decay of the signal at 516 nm; this wavelength was used since the background decomposition of the compound did not affect this wavelength.

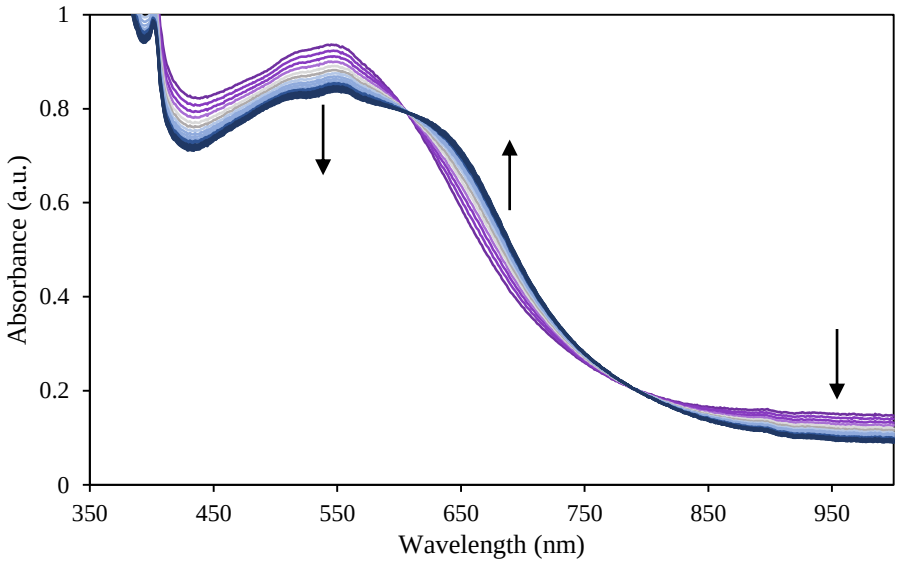

Figure S32. UV-Vis absorbance spectra of $LFe_3O(PzNHtBu)_3Fe(O)$ (**5**; 200 μM) and 9,10-dihydroanthracene (10 mM) at ambient temperature.

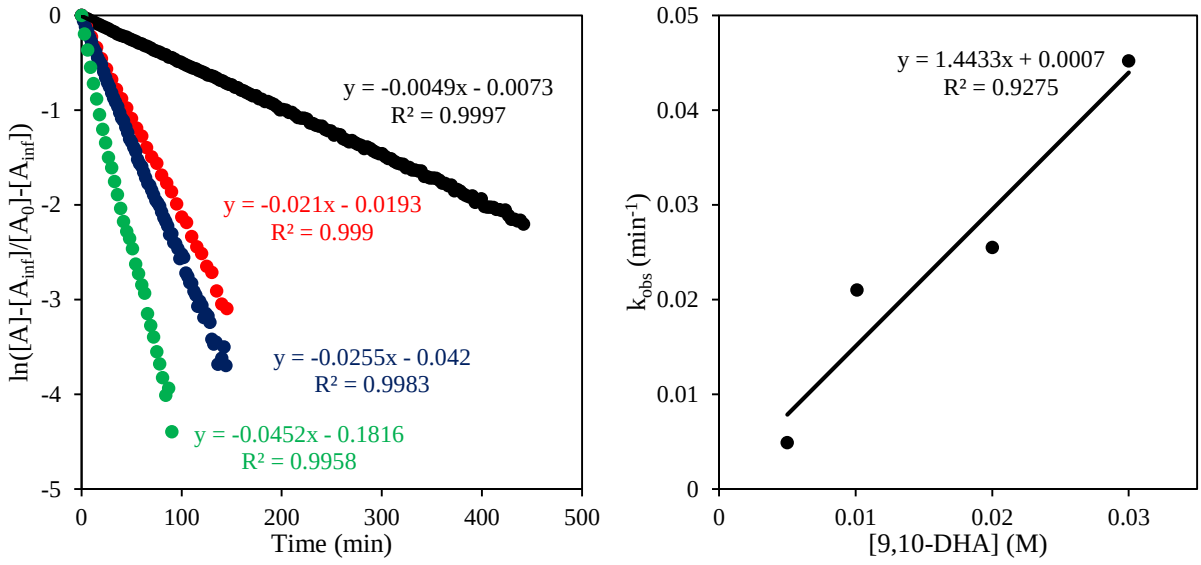

Figure S33. Kinetics data for the reaction between $LFe_3O(PzNHtBu)_3Fe(O)$ (**5**; 200 μM) and 9,10-dihydroanthracene (9,10-DHA; 5, 10, 20, and 30 mM) at ambient temperature. The decay of the UV-Vis absorbance feature at 540 nm was used to follow the reaction.

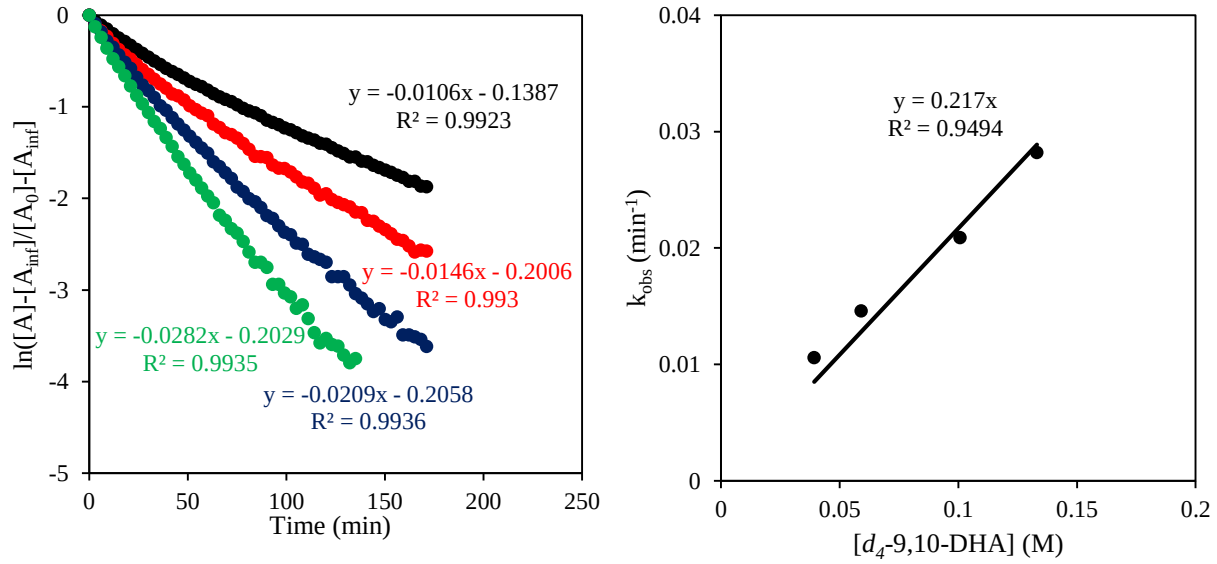

Figure S34. Kinetics data for the reaction between $LFe_3O(PzNHtBu)_3Fe(O)$ (**5**; 200 μM) and d_4-9,10-dihydroanthracene (d_4-9,10-DHA; 40, 60, 100, and 130 mM) at ambient temperature. The decay of the UV-Vis absorbance feature at 540 nm was used to follow the reaction.

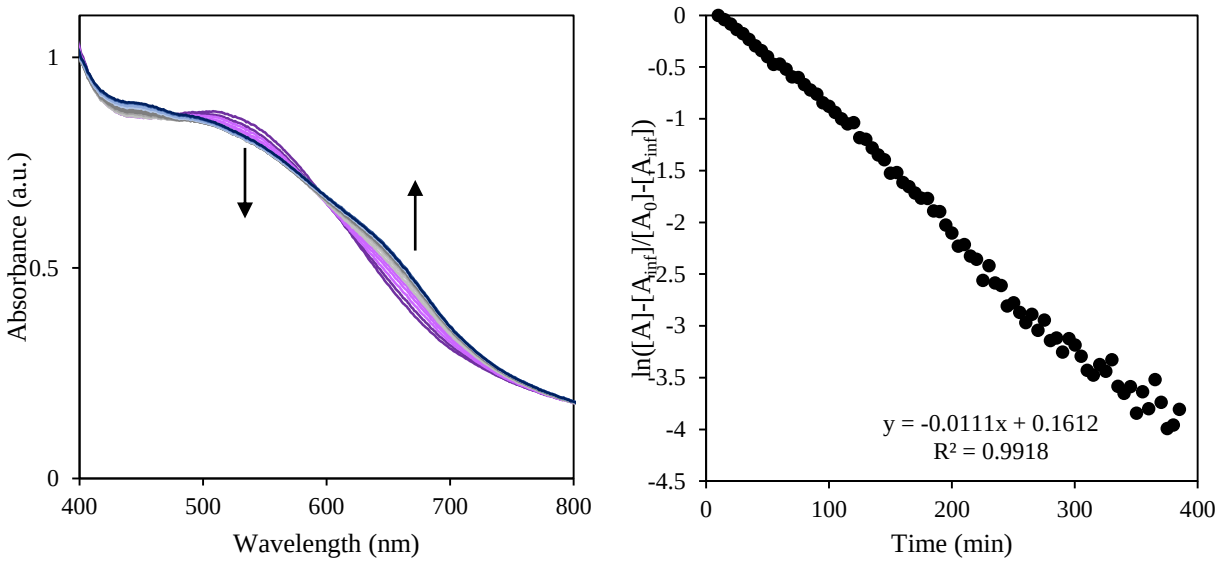

Figure S35. (Left) UV-Vis absorbance spectra of $LFe_3O(PzNHtBu)_3Fe(O)$ (**5**; 200 μM) and triphenylmethane (1 M) at ambient temperature. (Right) Pseudo-first order kinetics plot of the reaction by following the decay of the signal at 516 nm; this wavelength was used since the background decomposition of the compound did not affect this wavelength.

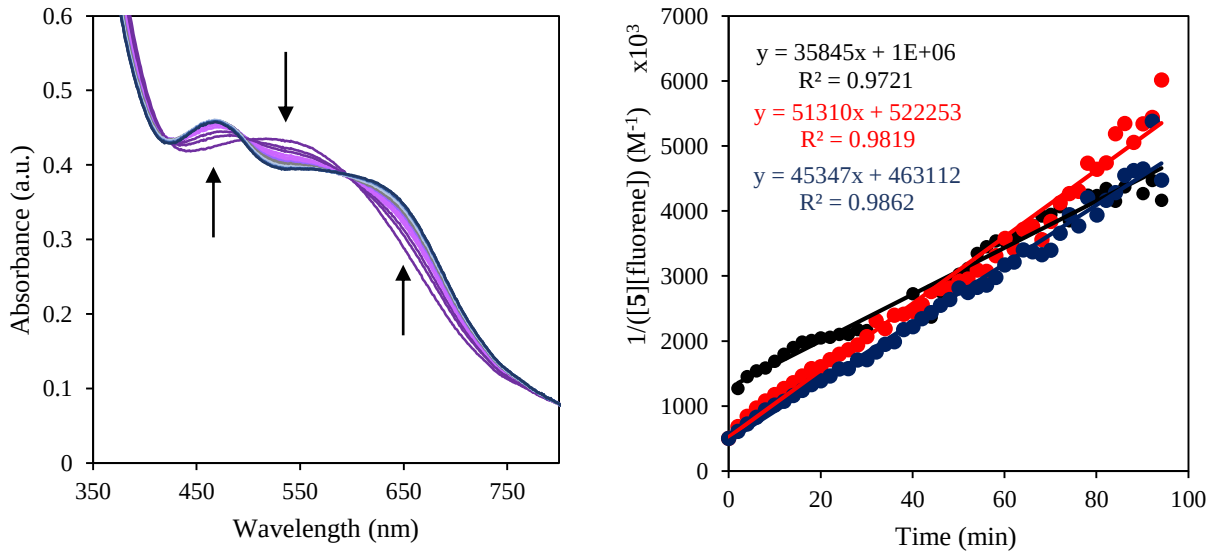

Figure S36. (Left) UV-Vis absorbance spectra of $LFe_3O(PzNHtBu)_3Fe(O)$ (**5**; 1 mM) and fluorene (2 mM) at ambient temperature in a 1 mm cuvette. (Right) Second order kinetics plot of the reaction by following the growth of the signal at 645 nm.

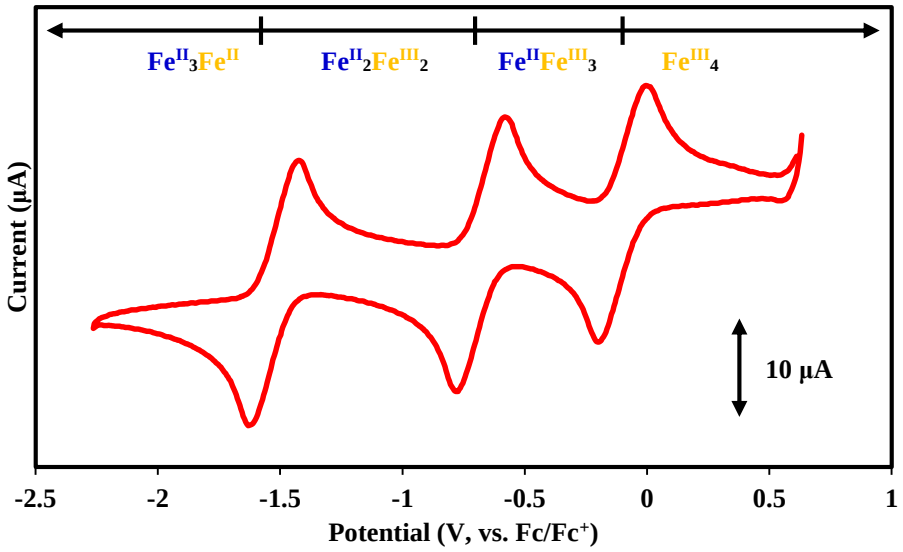

Figure S37. Cyclic voltammetry of $[LFe_3O(PzNHtBu)_3Fe(OH)][OTf]$, **2**, (2.5 mM) at 50 mV/s in THF with a glassy carbon working, platinum counter, and silver wire reference electrodes and ca. 200 mM $[Bu_4N][PF_6]$.

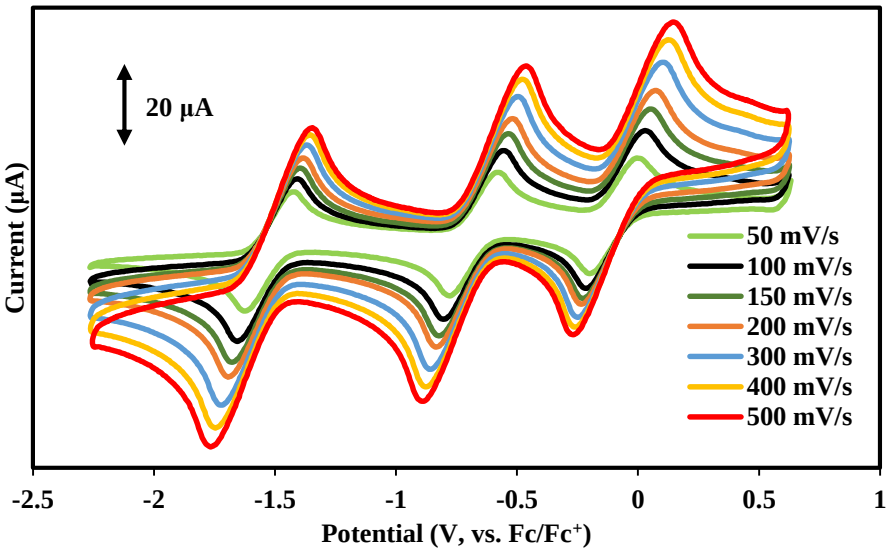

Figure S38. Cyclic voltammetry of $[LFe_3O(PzNHtBu)_3Fe(OH)][OTf]$, **2**, (2.5 mM) in THF with a glassy carbon working, platinum counter, and silver wire reference electrodes and ca. 200 mM $[Bu_4N][PF_6]$ at various scan rates.

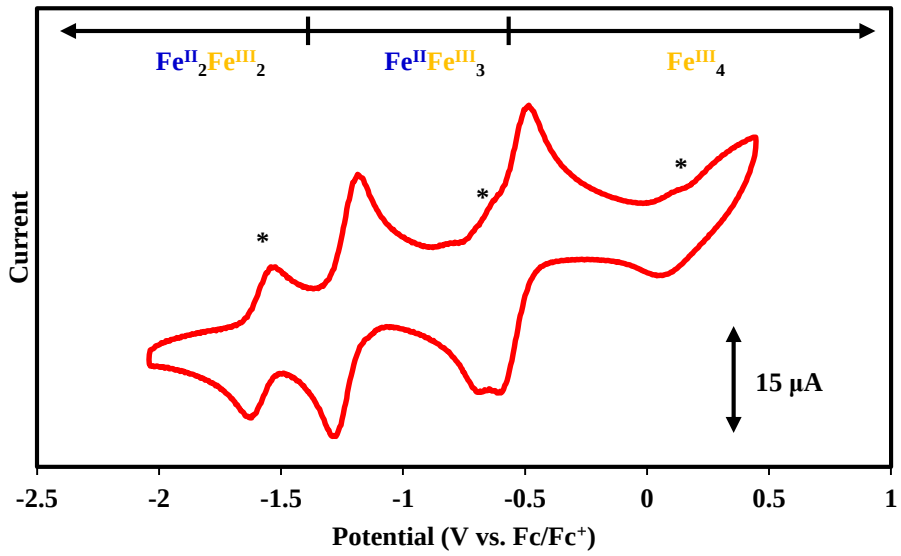

Figure S39. Cyclic voltammetry of $LFe_3O(PzNHtBu)_3Fe(O)$, **5,** (2.3 mM at 200 mV/s scan rate) in THF with a glassy carbon working, platinum counter, and silver wire reference electrodes and ca. 100 mM $[Bu_4N][PF_6]$. Electrochemical events marked with an asterisk (*) are assigned to a small amount of $[LFe_3O(PzNHtBu)_3Fe(OH)]^{n+}$ that formed due to decomposition.

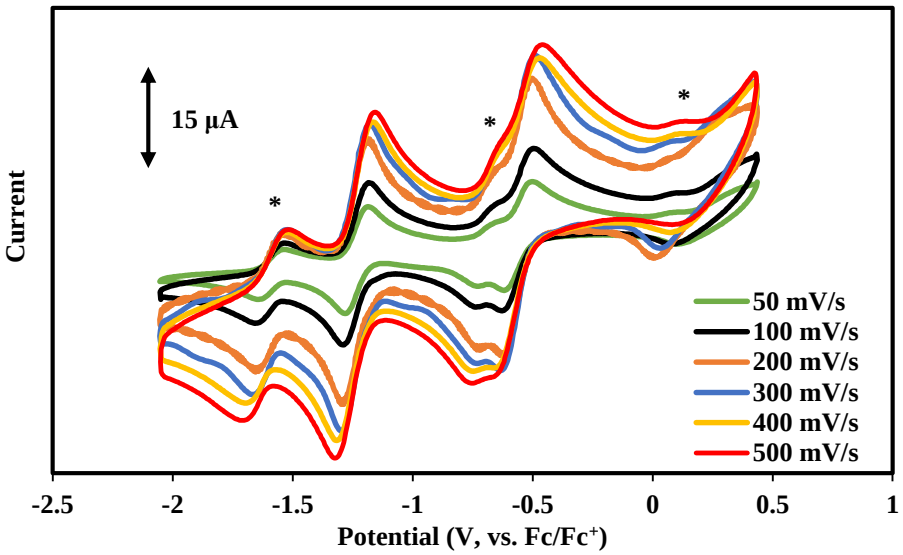

Figure S40. Cyclic voltammetry of $LFe_3O(PzNHtBu)_3Fe(O)$, **5**, (2.3 mM) in THF with a glassy carbon working, platinum counter, and silver wire reference electrodes and ca. 100 mM $[Bu_4N][PF_6]$ at various scan rates. Electrochemical events marked with an asterisk (*) are assigned to a small amount of $[LFe_3O(PzNHtBu)_3Fe(OH)]^{n+}$ that formed due to decomposition.

Mössbauer simulation details for all compounds. All spectra were simulated by four pairs of symmetric quadrupole doublets with equal populations and Lorentzian lineshapes. They were refined to a minimum via least squares optimization (13 fitting parameters per spectrum). Signals appearing above 2 mm/s were indicative with the presence of high-spin Fe^{II} centers and correspond to species with isomer shifts of ~ 1 mm/s. The Mössbauer data were fit to be consistent with our previously reported Fe clusters.[1, 14] The observed Mossbauer parameters are in agreement with related six-coordinate high-spin Fe^{II}/Fe^{III} centers.[15]

Simulation details for $LFe_3O(PzNHtBu)_3Fe(OH)$ (1): The spectrum displays three discernable peaks corresponding to two quadrupole doublets in ~ 1:3 ratio. The parameters of the more intense peak are consistent with a high-spin Fe(II) assignment, while the smaller doublet could be fit a number of ways, two of which are shown here (Figures S41 and S42). Figure S42 gives parameters most consistent with an apical Fe(III). The final fit split the large doublet into three equal signals (Figure S43).

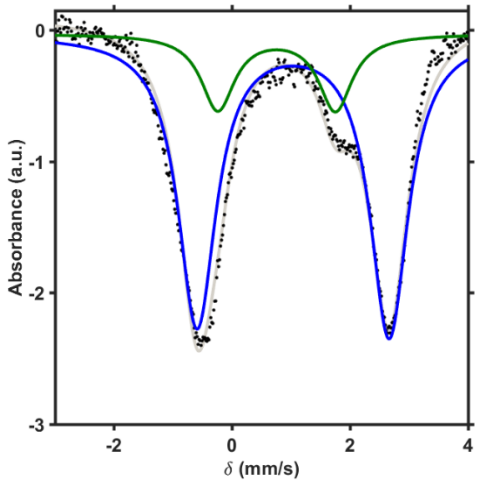

Figure S41. Mössbauer spectrum of **1** (black dots) fit with two doublets in a ~1:3 ratio (gray trace) with parameters δ = 1.035 mm/s; ΔE_q = 3.255 mm/s (blue trace) and δ = 0.756 mm/s; ΔE_q = 1.993 mm/s (green trace).

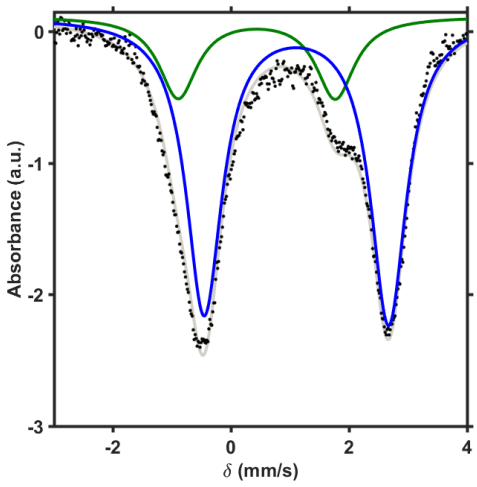

Figure S42. Mössbauer spectrum of **1** (black dots) fit with two doublets in a ~1:3 ratio (gray trace) with parameters δ = 1.107 mm/s; ΔE_q = 3.126 mm/s (blue trace) and δ = 0.436 mm/s; ΔE_q = 2.663 mm/s (green trace).

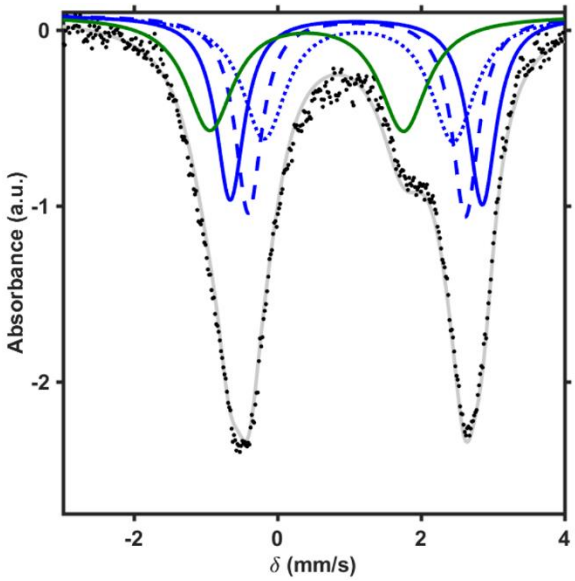

	δ (mm/s)	$\lvert\Delta E_q\rvert$ (mm/s)	Rel. %
———	1.099	3.519	25
– – –	1.109	3.029	25
- - - - -	1.134	2.640	25
———	0.407	2.706	25

Figure S43. Zero applied field Mössbauer spectrum of **1** (black dots) fit with four quadrupole doublets. The blue traces are assigned to high-spin Fe(II) and the green trace is assigned as Fe(III).

Simulation details for [LFe$_3$O(PzNHtBu)$_3$Fe(OH)][OTf] (2): The spectrum displays five discernable peaks corresponding to three quadrupole doublets in ~ 1:1:2 ratio. The parameters of the most intense peak are consistent with a high-spin Fe(II) assignment, and the remainder of the signal can be fit a number of ways (Figures S44 and S45). Figure S45 gives parameters most consistent with an apical Fe(III). The final fit split the large doublet into two equal signals (Figure S46).

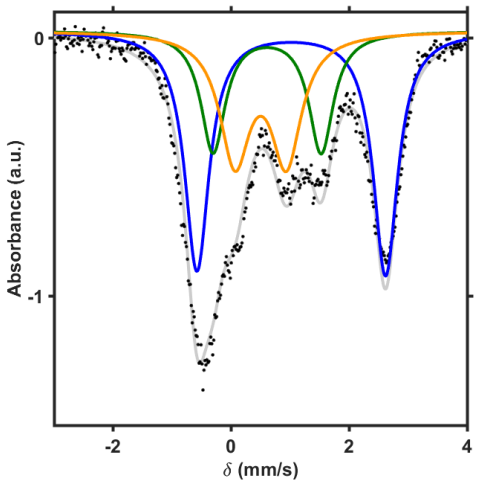

Figure S44. Mössbauer spectrum of **2** (black dots) fit with three doublets in a ~1:1:2 ratio (gray trace) with parameters δ = 1.020 mm/s; ΔE_q = 3.197 mm/s (blue trace), δ = 0.502 mm/s; ΔE_q = 0.871 mm/s (orange trace) and δ = 0.612 mm/s; ΔE_q = 1.832 mm/s (green trace).

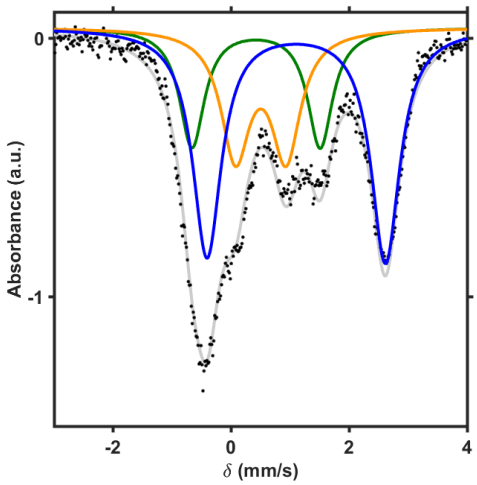

Figure S45. Mössbauer spectrum of **2** (black dots) fit with three doublets in a ~1:1:2 ratio (gray trace) with parameters δ = 1.107 mm/s; ΔE_q = 3.126 mm/s (blue trace), δ = 0.504 mm/s; ΔE_q = 0.857 mm/s (orange trace) and δ = 0.425 mm/s; ΔE_q = 2.172 mm/s (green trace).

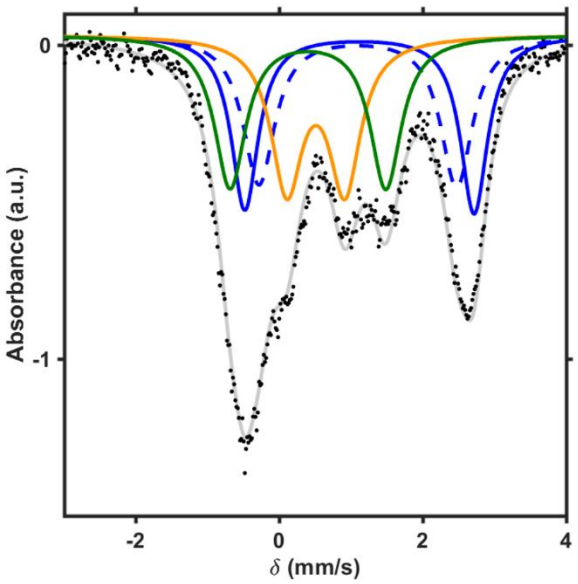

	δ (mm/s)	$\lvert\Delta E_q\rvert$ (mm/s)	Rel. %
———	1.123	3.197	25
- - -	1.100	2.757	25
———	0.515	0.809	25
———	0.406	2.171	25

Figure S46. Zero applied field Mössbauer spectrum of **2** (black dots) fit with four quadrupole doublets. The blue traces are assigned to high-spin Fe(II), the orange trace is assigned to high-spin Fe(III), and the green trace is assigned as Fe(III).

Simulation details for [LFe$_3$O(PzNHtBu)$_3$Fe(OH)][OTf]$_2$ (3): The spectrum displays three discernable peaks corresponding to two quadrupole doublets in ~ 1:3 ratio. The parameters of the less intense peak are consistent with a high-spin Fe(II) assignment, and the remainder of the signal can be fit a number of ways. Based on the Mossbauer parameters for the other cluster oxidation states (Figure S43 and S46), a fit was performed to obtain self-consistent parameters (i.e. making apical Fe(III) doublet with second largest quadrupole splitting). This fit led to parameters that are in good agreement for a high-spin Fe(II), two high-spin Fe(III), and the unique apical Fe(III) environment (Figure S47).

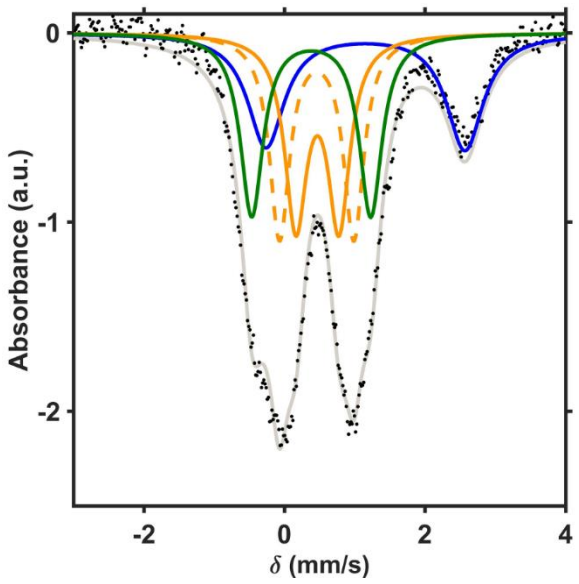

	δ (mm/s)	$\lvert\Delta E_q\rvert$ (mm/s)	Rel. %
	1.153	2.829	25
	0.469	0.613	25
	0.459	1.056	25
	0.381	1.693	25

Figure S47. Zero applied field Mössbauer spectrum of **3** (black dots) fit with four quadrupole doublets. The blue trace is assigned to high-spin Fe(II), the orange traces are assigned to high-spin Fe(III), and the green trace is assigned as Fe(III).

Simulation details for [LFe$_3$O(PzNHtBu)$_3$Fe(OH)][OTf]$_3$ (4): The spectrum displays two peaks of different intensities and shapes, consistent with multiple overlapping quadrupole doublets. In order to obtain self-consistent parameters, the spectrum was fit to four quadrupole doublets, with the doublet with the highest quadrupole splitting assigned to the apical Fe(III) (Figure S48).

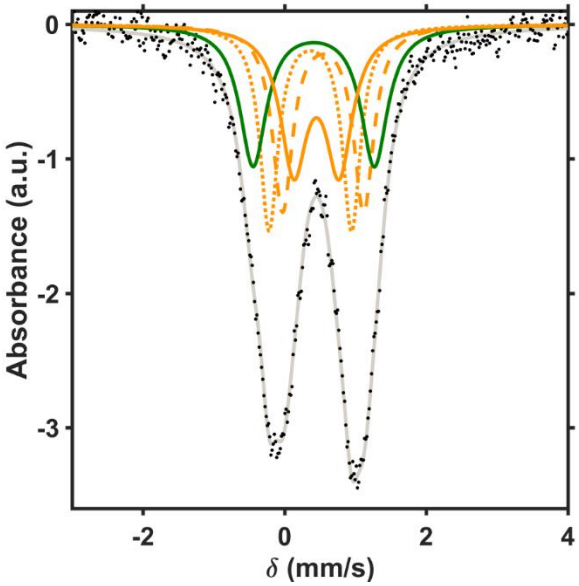

	δ (mm/s)	$\lvert\Delta E_q\rvert$ (mm/s)	Rel. %
	0.449	0.641	25
	0.543	1.145	25
	0.363	1.166	25
	0.411	1.712	25

Figure S48. Zero applied field Mössbauer spectrum of **4** (black dots) fit with four quadrupole doublets. The orange traces are assigned to high-spin Fe(III) and the green trace is assigned as Fe(III).

Simulation details for $LFe_3O(PzNHtBu)_3Fe(O)$ (5): The spectrum displays six discernable peaks corresponding to three quadrupole doublets in ~ 1:1:2 ratio. The parameters of the most intense peak are consistent with a high-spin Fe(II) assignment, and the remainder of the signal can be fit a number of ways (Figures S49, S50, and S51). Figure S51 gives parameters most consistent with an apical Fe(III) and high-spin Fe(III) in the tri-iron core. The final fit split the large doublet into two equal signals (Figure S52).

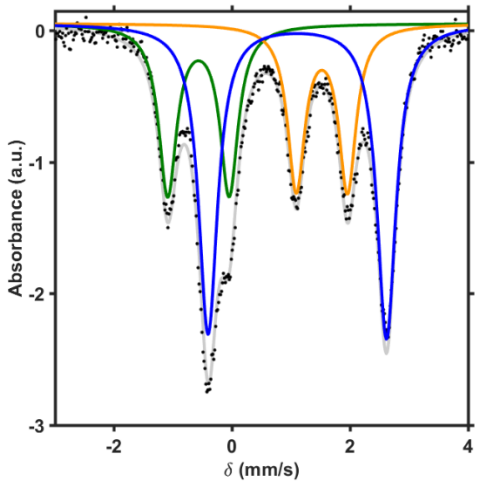

Figure S49. Mössbauer spectrum of **5** (black dots) fit with three doublets in a ~1:1:2 ratio (gray trace) with parameters δ = 1.106 mm/s; ΔE_q = 3.023 mm/s (blue trace), δ = 1.522 mm/s; ΔE_q = 0.868 mm/s (orange trace) and δ = -0.569 mm/s; ΔE_q = 1.042 mm/s (green trace).

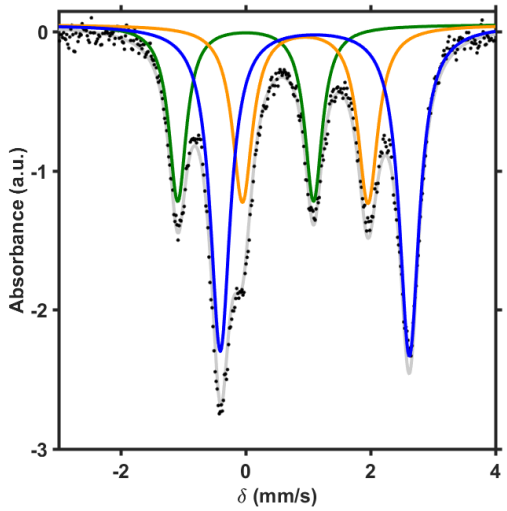

Figure S50. Mössbauer spectrum of **5** (black dots) fit with three doublets in a ~1:1:2 ratio (gray trace) with parameters δ = 1.106 mm/s; ΔE_q = 3.029 mm/s (blue trace), δ = 0.952 mm/s; ΔE_q = 2.010 mm/s (orange trace) and δ = -0.003 mm/s; ΔE_q = 2.178 mm/s (green trace).

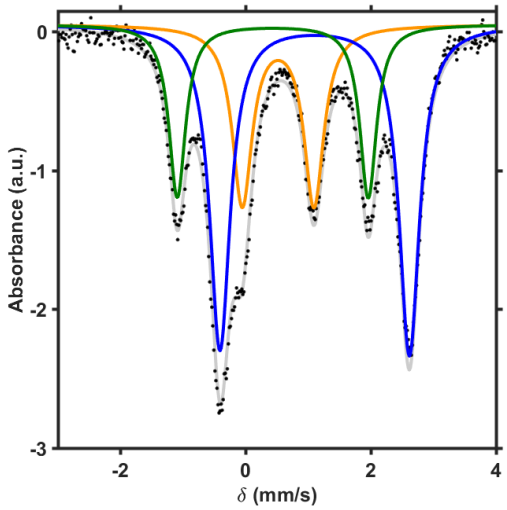

Figure S51. Mössbauer spectrum of **5** (black dots) fit with three doublets in a ~1:1:2 ratio (gray trace) with parameters δ = 1.103 mm/s; ΔE_q = 3.027 mm/s (blue trace), δ = 0.518 mm/s; ΔE_q = 1.146 mm/s (orange trace) and δ = 0.432 mm/s; ΔE_q = 3.051 mm/s (green trace).

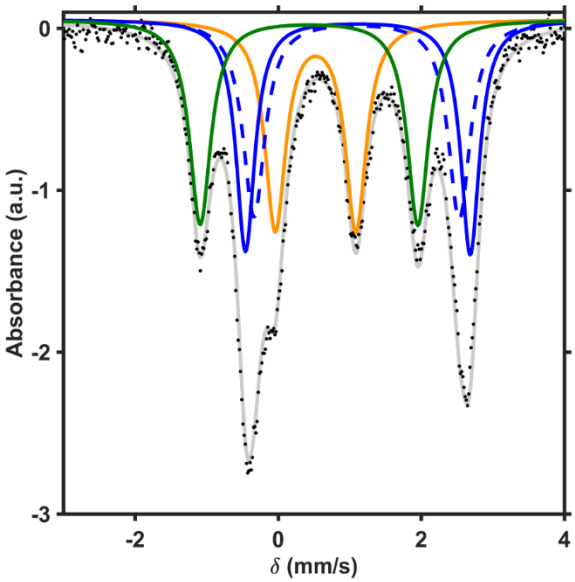

	δ (mm/s)	$\lvert\Delta E_q\rvert$ (mm/s)	Rel. %
———	1.115	3.141	25
– – –	1.097	2.869	25
———	0.524	1.126	25
———	0.433	3.042	25

Figure S52. Zero applied field Mössbauer spectrum of **5** (black dots) fit with four quadrupole doublets. The blue traces are assigned to high-spin Fe(II), the orange trace is assigned to high-spin Fe(III), and the green trace is assigned to Fe(III).

Simulation details for [LFe$_3$O(PzNHtBu)$_3$Fe(O)][OTf] (6): The spectrum displays five discernable peaks corresponding to three quadrupole doublets in ~ 1:1:2 ratio. The parameters of the most intense peak are consistent with a high-spin Fe(III) assignment, and the remainder of the signal can be fit a number of ways (Figures S53 and S54). Figure S54 gives parameters most consistent with an apical Fe(III). The final fit split the large doublet into two equal signals (Figure S55).

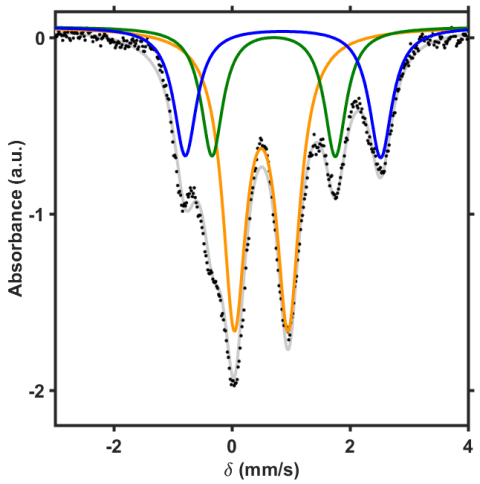

Figure S53. Mössbauer spectrum of **6** (black dots) fit with three doublets in a ~1:1:2 ratio (gray trace) with parameters δ = 0.864 mm/s; ΔE_q = 3.311 mm/s (blue trace), δ = 0.495 mm/s; ΔE_q = 0.912 mm/s (orange trace) and δ = 0.706 mm/s; ΔE_q = 2.089 mm/s (green trace).

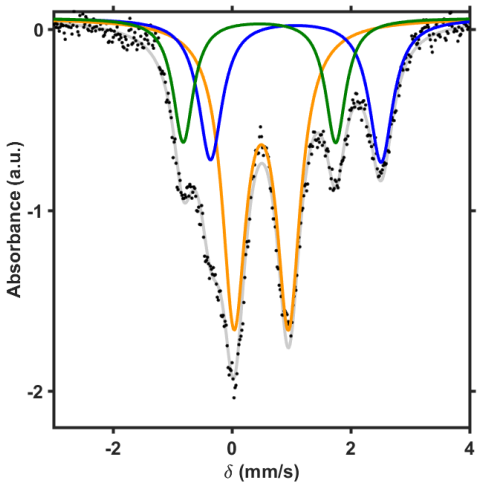

Figure S54. Mössbauer spectrum of **6** (black dots) fit with three doublets in a ~1:1:2 ratio (gray trace) with parameters δ = 1.077 mm/s; ΔE_q = 2.870 mm/s (blue trace), δ = 0.496 mm/s; ΔE_q = 0.916 mm/s (orange trace) and δ = 0.465 mm/s; ΔE_q = 2.565 mm/s (green trace).

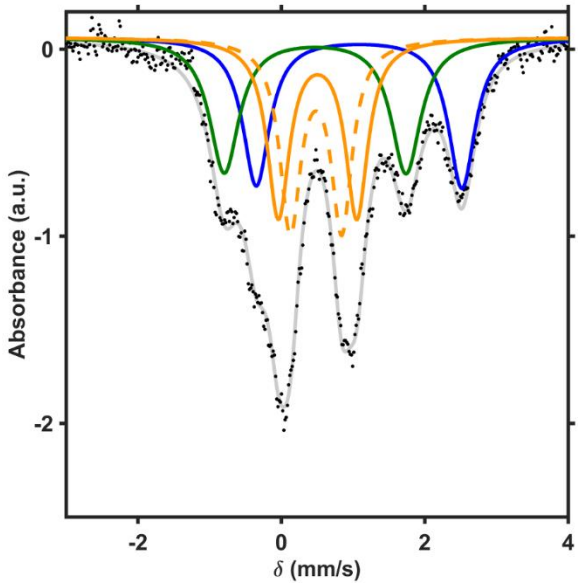

	δ (mm/s)	$\lvert\Delta E_q\rvert$ (mm/s)	Rel. %
———	1.085	2.867	25
———	0.507	1.093	25
- - -	0.485	0.717	25
———	0.473	2.532	25

Figure S55. Zero applied field Mössbauer spectrum of **6** (black dots) fit with four quadrupole doublets. The blue trace is assigned to high-spin Fe(II), the orange traces are assigned to high-spin Fe(III), and the green trace is assigned to Fe(III).

Simulation details for $[LFe_3O(PzNHtBu)_3Fe(O)][OTf]_2$ (7): The small peak at >2 mm/s indicated the presence of a FeII-containing impurity; NMRs of this cluster typically contained $[LFe_3O(PzNHtBu)_3Fe(OH)][OTf]_2$ (**3**) as an impurity (Figures S47 and S56). Using the parameters for **3** above, the Fe^{II} doublet was used to estimate the amount of this impurity (30 – 40% of the spectrum). This was subtracted from the data, and the remaining data appeared to be one broad doublet, similar to the $[Fe^{III}_4]$ spectrum of **4**. It was fit as four equal doublets, with the apical Fe(III) tentatively assigned to the doublet with the highest quadrupole splitting, to represent the highest value possible for this parameter (Figure S57). 1H NMR of the Mössbauer sample after collection is consistent with the presence of **3** and **7** (Figure S58).

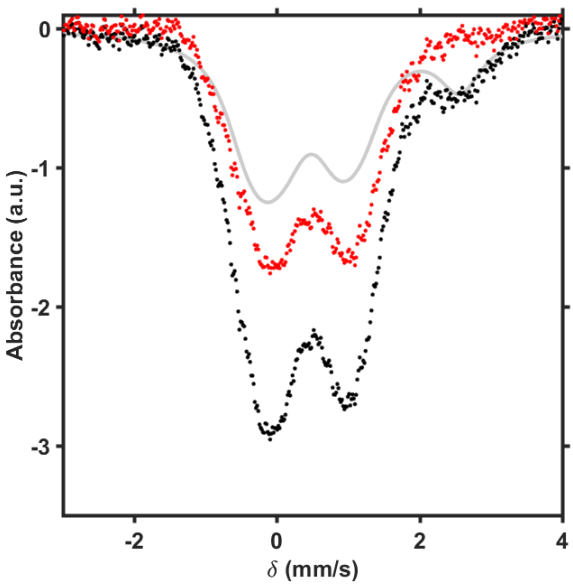

Figure S56. Mössbauer spectrum of reaction mixture containing **7** and **3** (black dots) fit with parameters to account for **3** (gray trace). The remaining signal (red dots) is assigned to the Mossbauer signal of **7**.

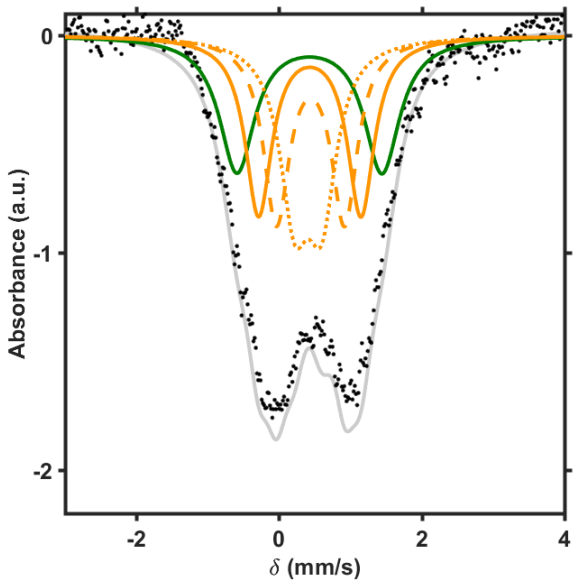

	δ (mm/s)	$\lvert\Delta E_q\rvert$ (mm/s)	Rel. %
———	0.430	1.435	25
– – –	0.440	0.953	25
·····	0.407	0.379	25
———	0.426	2.033	25

Figure S57. Zero applied field Mössbauer spectrum of **7** (black dots) fit with four quadrupole doublets. The orange traces are assigned to high-spin Fe(III), and the green trace is assigned to the unique Fe(III).

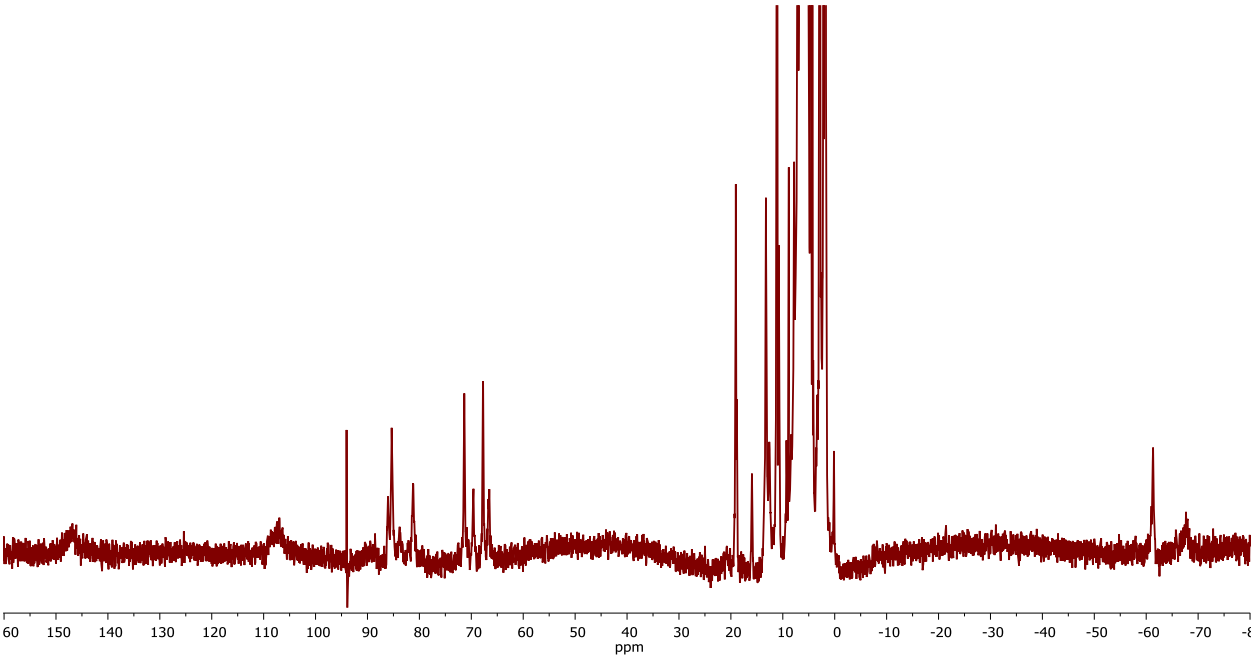

Figure S58. ^{1}H NMR spectrum (300 MHz) of Mössbauer sample after collection in CD_3CN. The peaks of the major species match that of **7**, while the impurity corresponds to **3**. The sharp peak ~ 95 ppm is a spectral artifact.

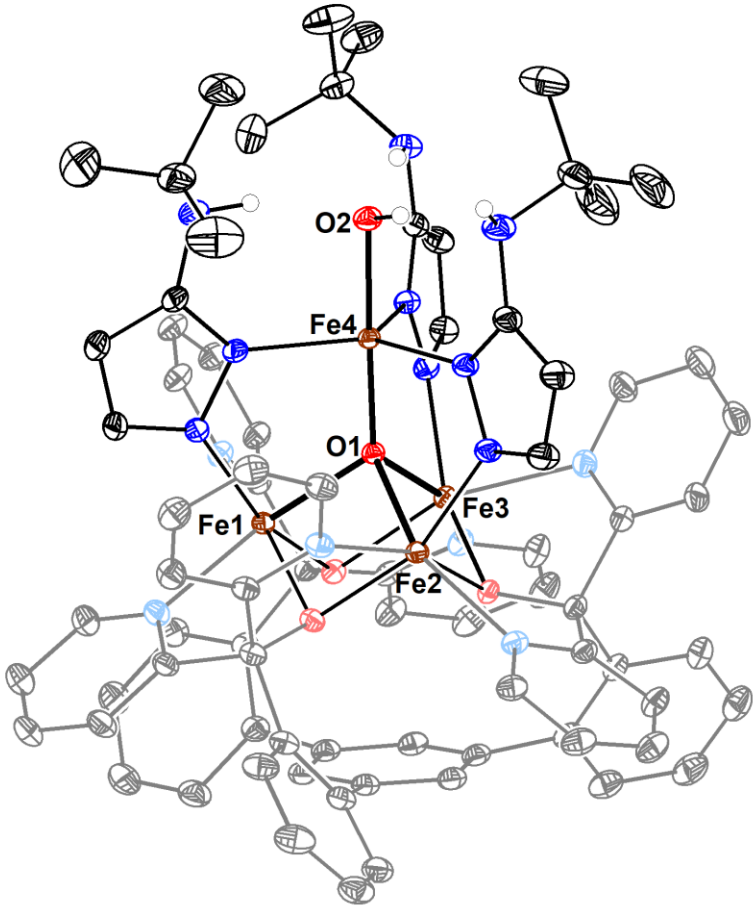

Figure S59. Crystal structure of $LFe_3O(PzNHtBu)_3Fe(OH)$ (**1**). Ellipsoids are shown at the 50% probability level. Hydrogen atoms and solvent molecules removed for clarity.

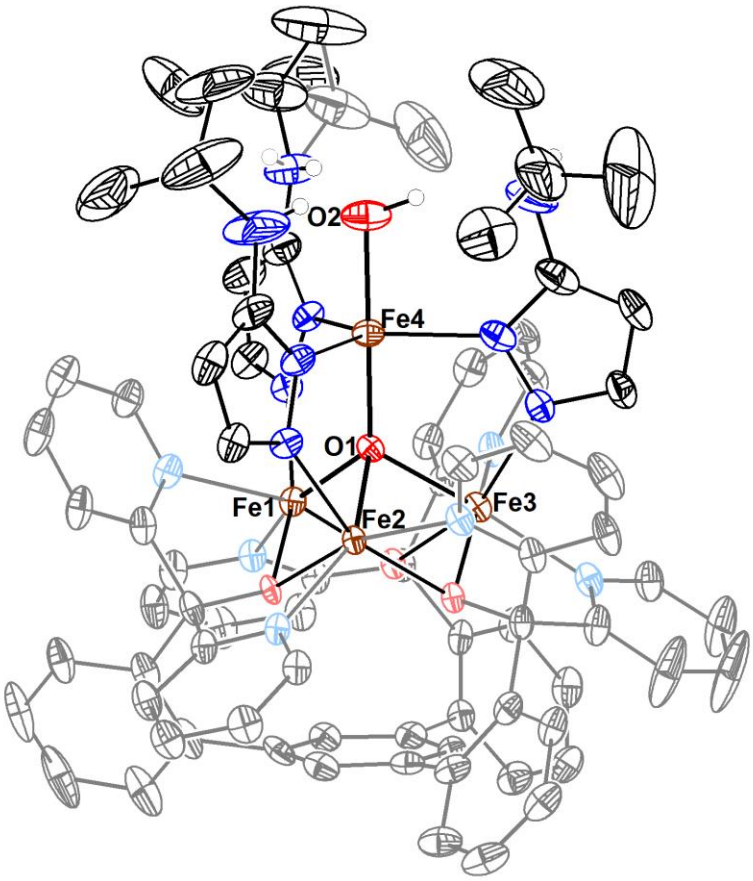

Figure S60. Crystal structure of [$LFe_3O(PzNHtBu)_3Fe(OH)][PF_6]$ (**2-PF_6**). Ellipsoids are shown at the 50% probability level. Hydrogen atoms and solvent molecules removed for clarity.

Special refinement details for [$LFe_3O(PzNHtBu)_3Fe(OH)][PF_6]$. A *tert*-butyl group of one of the pyrazolate ligands is partially disordered over two positions with occupancies of 39% (C93 and C94) and 61% (C97 and C98). There is significant solvent disorder that could not be fully refined, however electron density for a tetrahydrofuran (O100 and C100-C103), and two partial diethyl ether molecules (refined as C104-C109) were refined isotropically with only partial occupancy.

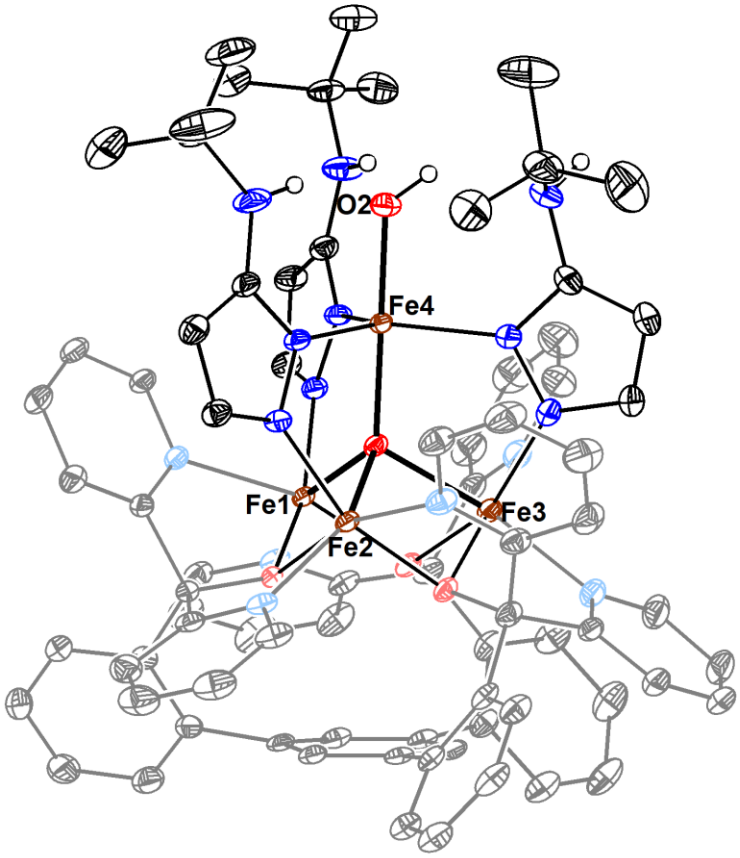

Figure S61. Crystal structure of $[LFe_3O(PzNHtBu)_3Fe(OH)][OTf]_2$ (**3**). Ellipsoids are shown at the 50% probability level. Hydrogen atoms and solvent molecules removed for clarity.

Special refinement details for $[LFe_3O(PzNHtBu)_3Fe(OH)][OTf]_2$. One of the outersphere triflates was modeled as disordered over two nearly identical positions, with occupancies of 75% (S101 through C101) and 25% (S102 through C102). A 'SAME' constraint was used to favor distances and angles of these disordered triflates to the non-disordered one. A partially occupied solvent molecule (likely Et_2O) was present; however, due to its position near a symmetry element, its residual electron density was removed via a solvent mask, as opposed to modeling this disordered solvent.

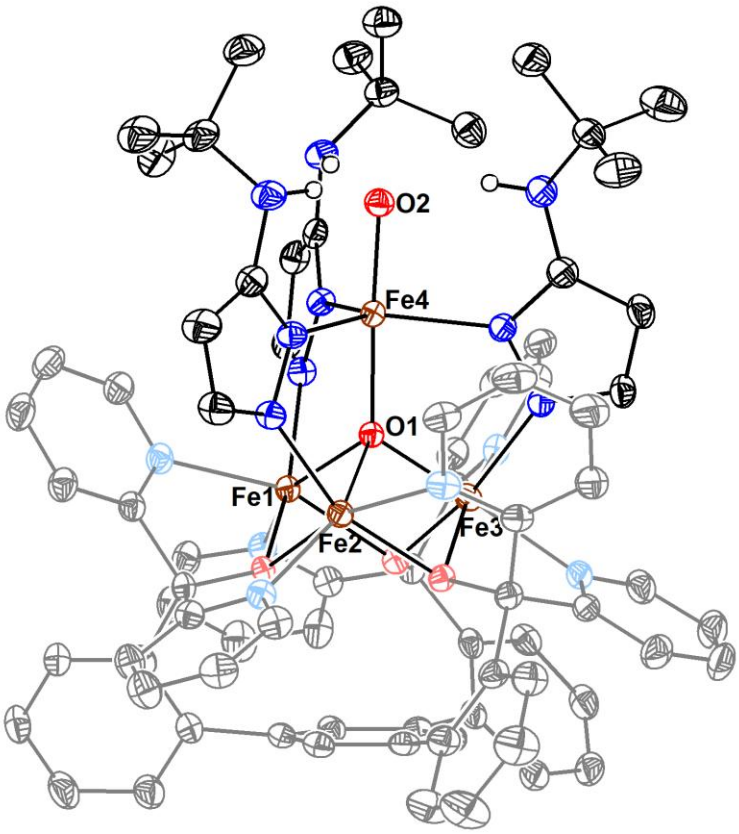

Figure S62. Crystal structure of $LFe_3O(PzNHtBu)_3Fe(O)$ (**5**). Ellipsoids are shown at the 50% probability level. Hydrogen atoms and solvent molecules removed for clarity.

Special refinement details for $[LFe_3O(PzNHtBu)_3Fe(O)]$. A benzene solvent is positionally disordered over two positions with occupancies of 29% (C106-C111) and 71% (C206-C211).

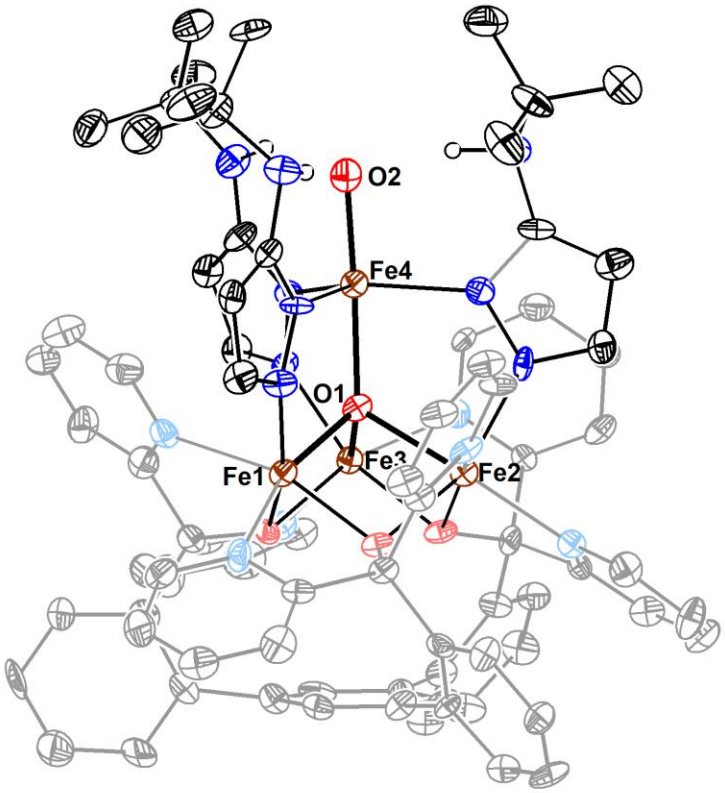

Figure S63. Crystal structure of [$LFe_3O(PzNHtBu)_3Fe(O)$][OTf] (**6**). Ellipsoids are shown at the 50% probability level. Hydrogen atoms, outersphere counterion, and solvent molecules removed for clarity.

Special refinement details for [$LFe_3O(PzNHtBu)_3Fe(O)$][OTf]. Generally, these crystals were of relatively poor quality compared to the other structures obtained; the crystal was twinned with a 13% twinned crystal component. While no disorder had to be modeled in the molecule, the outerphere triflate, or the three additional molecules of THF, the low intensity of high angle diffraction data led to low C–C bond precision. Initially, some carbon atoms in the ligand backbone had highly skewed ellipsoids, which were addressed with SIMU/DELU restraints (on O11, C11, C12, C26, C27, and C42 – C45) or, in one case, an ISOR restraint (C44).

Bond Distance (Å)	**1**	**2-PF_6**	**3**	**5**	**6**
Fe1–O1	2.102(1)	2.142(3)	2.148(1)	2.139(1)	2.154(7)
Fe2–O1	2.109(1)	2.101(3)	2.002(2)	2.050(2)	1.927(7)
Fe3–O1	2.089(1)	1.952(3)	1.971(1)	1.967(2)	1.948(7)
Fe4–O1	1.837(1)	1.890(3)	1.948(2)	1.965(2)	2.049(7)
Fe4–O2	1.937(1)	1.907(3)	1.879(2)	1.817(2)	1.795(8)
Fe1–N13	2.129(1)	2.107(4)	2.074(2)	2.124(2)	2.091(9)
Fe2–N23	2.126(1)	2.106(3)	2.057(2)	2.084(2)	2.039(9)
Fe3–N33	2.120(1)	2.071(4)	2.017(2)	2.090(2)	2.015(8)
Fe4–N14	2.097(1)	2.091(4)	2.083(2)	2.093(2)	2.085(9)
Fe4–N24	2.168(1)	2.056(4)	2.047(2)	2.104(2)	2.087(9)
Fe4–N34	2.111(1)	2.105(4)	2.059(2)	2.098(2)	2.100(8)
N13–N14	1.382(1)	1.373(5)	1.377(2)	1.388(2)	1.396(12)
N23–N24	1.368(1)	1.387(5)	1.394(2)	1.387(3)	1.384(11)
N33–N34	1.386(1)	1.389(5)	1.397(2)	1.378(3)	1.387(12)
N15–C72	1.397(2)	1.417(7)	1.422(3)	1.400(3)	1.379(14)
N25–C82	1.422(2)	1.354(7)	1.356(3)	1.366(5)	1.391(14)
(N26–C82)	-	-	-	1.41(2)	-
N35–C92	1.393(2)	1.383(7)	1.350(3)	1.402(3)	1.341(14)
Bond Angles (º)					
N14–Fe4–N24	120.1	119.1	116.6	118.3	113.4
N24–Fe4–N34	122.1	118.8	119.8	123.0	119.6
N34–Fe4–N14	117.8	121.7	122.7	117.5	124.0
N14–Fe4–O2	88.4	91.7	92.6	96.3	97.6
N24–Fe4–O2	91.3	93.5	95.0	92.0	96.3
N34–Fe4–O2	92.2	91.1	92.1	92.8	93.6
O1–Fe4–O2	177.1	177.3	178.7	177.1	176.0
Torsion Angles (º)					
Fe1–N13–N14–Fe4	13.9	2.7	6.2	19.4	21.9
Fe2–N23–N24–Fe4	11.6	9.9	8.2	4.5	17.4
Fe3–N33–N34–Fe4	13.4	12.5	11.1	13.7	2.7
Centroid Distances (Å)					
Fe1|Fe2|Fe3–N14|N24|N34	2.050	1.701	1.643	1.685	1.627
Fe1|Fe2|Fe3–O11|O21|O31	1.121	1.110	1.078	1.120	1.122
Fe1|Fe2|Fe3–O1	1.153	1.105	1.036	1.076	1.012
N14|N24|N34–Fe4	0.025	0.075	0.120	0.138	0.218

Table S5. Selected bond parameters for structurally characterized compounds **1**-**3**, **5**, and **6**.

	1	**2-PF_6**	**3**
CCDC Number	1903350	1903348	1903352
Empirical	$C_{90}H_{88}Fe_4N_{15}O_5$	$C_{83}H_{76}F_6Fe_4N_{15}O_{5.5}P$	$C_{80}H_{76}F_6Fe_4N_{15}O_{11}S_2$
Formula weight	1683.15	1793.95	1825.07
Radiation	MoKα (λ = 0.71073)	CuKα (λ = 1.54178)	CuKα (λ = 1.54178)
a (Å)	14.1115(11)	11.9919(11)	12.150(2)
b (Å)	15.0509(11)	13.7630(9)	14.975(5)
c (Å)	21.1556(16)	25.905(2)	23.386(6)
α (°)	70.794(3)	89.286(4)	95.271(14)
β (°)	86.911(3)	87.757(4)	90.124(12)
γ (°)	70.570(3)	79.589(4)	104.172(19)
V (Å^3)	3993.7(5)	4201.8(6)	4106.5(18)
Z	2	2	2
Cryst. syst.	triclinic	triclinic	triclinic
Space group	P-1	P-1	P-1
ρ_{calc}g (cm^3)	1.400	1.375	1.476
2 σ range (°)	4.74 to 77.068	6.53 to 149.628	3.796 to 148.742
μ (mm^{-1})	0.777	6.219	6.726
GOF	1.019	1.044	1.063
R1, wR2 (I>2σ (I))	0.0412, 0.0980	0.0710, 0.1919	0.0375, 0.0940

	5	**6**
CCDC Number	1903351	1903349
Empirical formula	$C_{90}H_{87}Fe_4N_{15}O_5$	$C_{91}H_{99}F_3Fe_4N_{15}O_{11}S$
Formula weight	1682.14	1673.00
Radiation	CuKα (λ=1.54178)	CuKα (λ=1.54178)
a (Å)	12.3162(13)	19.122(9)
b (Å)	15.5743(15)	18.204(5)
c (Å)	21.6599(15)	24.698(6)
α (°)	102.390(6)	90
β (°)	94.445(4)	90
γ (°)	102.897(9)	90
V (Å^3)	3921.5(7)	8597(5)
Z	2	4
Cryst. syst.	triclinic	orthorhombic
Space group	P-1	$Pna2_1$
ρ_{calc}g (cm^3)	1.425	1.463
2 σ range (°)	6.454 to 160.188	6.032 to 130.72
μ (mm^{-1})	6.338	6.172
GOF	1.012	1.064
R1, wR2 (I>2σ (I))	0.0400, 0.0954	0.0732, 0.1352

Table S6. Crystal and refinement data for complexes.

References

1. de Ruiter, G.; Thompson, N. B.; Lionetti, D.; Agapie, T. *J. Am. Chem. Soc.* **2015,** *137*, 14094-14106.
2. Huang, C.-Y.; Doyle, A. G. *J. Am. Chem. Soc.* **2012,** *134*, 9541-9544.
3. Izod, K.; Rayner, D. G.; El-Hamruni, S. M.; Harrington, R. W.; Baisch, U. *Angew. Chem. Int. Ed.* **2014,** *53*, 3636-3640.
4. Hagadorn, J. R.; Que, L.; Tolman, W. B. *Inorg. Chem.* **2000,** *39*, 6086-6090.
5. Adhikari, D.; Mossin, S.; Basuli, F.; Huffman, J. C.; Szilagyi, R. K.; Meyer, K.; Mindiola, D. J. *J. Am. Chem. Soc.* **2008,** *130*, 3676-3682.
6. Ludwiczak, M.; Majchrzak, M.; Marciniec, B.; Kubicki, M. *J. Organomet. Chem.* **2011,** *696*, 1456-1464.
7. Alberola, A.; Antolín, L. F.; Cuadrado, P.; González, A. M.; Laguna, M. A.; Pulido, F. J. *Synthesis* **1988,** *1988*, 203-207.
8. (a) Saame, J.; Rodima, T.; Tshepelevitsh, S.; Kütt, A.; Kaljurand, I.; Haljasorg, T.; Koppel, I. A.; Leito, I. *The Journal of Organic Chemistry* **2016,** *81*, 7349-7361; (b) Garrido, G.; Koort, E.; Ràfols, C.; Bosch, E.; Rodima, T.; Leito, I.; Rosés, M. *The Journal of Organic Chemistry* **2006,** *71*, 9062-9067.
9. Lionetti, D.; Suseno, S.; Tsui, E. Y.; Lu, L.; Stich, T. A.; Carsch, K. M.; Nielsen, R. J.; Goddard, W. A.; Britt, R. D.; Agapie, T. *Inorg. Chem.* **2019,** *58*, 2336-2345.
10. Xue, X.-S.; Ji, P.; Zhou, B.; Cheng, J.-P. *Chem. Rev.* **2017,** *117*, 8622-8648.
11. Bordwell, F. G.; Bares, J. E.; Bartmess, J. E.; McCollum, G. J.; Van der Puy, M.; Vanier, N. R.; Matthews, W. S. *The Journal of Organic Chemistry* **1977,** *42*, 321-325.
12. Matthews, W. S.; Bares, J. E.; Bartmess, J. E.; Bordwell, F. G.; Cornforth, F. J.; Drucker, G. E.; Margolin, Z.; McCallum, R. J.; McCollum, G. J.; Vanier, N. R. *J. Am. Chem. Soc.* **1975,** *97*, 7006-7014.
13. Taskinen, E.; Nummelin, K. *The Journal of Organic Chemistry* **1985,** *50*, 4844-4847.
14. (a) de Ruiter, G.; Thompson, N. B.; Takase, M. K.; Agapie, T. *J. Am. Chem. Soc.* **2016,** *138*, 1486-1489; (b) Herbert, D. E.; Lionetti, D.; Rittle, J.; Agapie, T. *J. Am. Chem. Soc.* **2013,** *135*, 19075-19078; (c) de Ruiter, G.; Carsch, K. M.; Gul, S.; Chatterjee, R.; Thompson, N. B.; Takase, M. K.; Yano, J.; Agapie, T. *Angew. Chem. Int. Ed.* **2017,** *56*, 4772-4776.
15. (a) Herold, S.; Lippard, S. J. *Inorg. Chem.* **1997,** *36*, 50-58; (b) Singh, A. K.; Jacob, W.; Boudalis, A. K.; Tuchagues, J.-P.; Mukherjee, R. *Eur. J. Inorg. Chem.* **2008,** *2008*, 2820-2829; (c) Sutradhar, M.; Carrella, L. M.; Rentschler, E. *Eur. J. Inorg. Chem.* **2012,** *2012*, 4273-4278; (d) Schünemann, V.; Hauke, P. Mössbauer Spectroscopy. In *Applications of Physical Methods to Inorganic and Bioinorganic Chemistry*, Scott, R. A.; Lukehart, C. M., Eds. John Wiley & Sons: West Sussex, England, 2007; pp 243-269.